IN VIVO OPTICAL IMAGING OF BRAIN FUNCTION

Edited by
Ron D. Frostig

CRC PRESS
Boca Raton London New York Washington, D.C.

CRC PRESS
Boca Raton London New York Washington, D.C.

Library of Congress Cataloging-in-Publication Data

Frostig, Ron D.
In vivo optical imaging of brain function / Ron D. Frostig.
p. ; cm. — (Methods & new frontiers in neuroscience)
Includes bibliographical references and index.
ISBN 8493-2389-4
1. Brain—Imaging. I. Title. II. Series.
[DNLM: 1. Brain—physiology. 2. Diagnostic Imaging. WL 300 F939i 2002]
QP376.6 .F765 2002
612.8'2—dc21 2002019238
CIP

This book contains information obtained from authentic and highly regarded sources. Reprinted material is quoted with permission, and sources are indicated. A wide variety of references are listed. Reasonable efforts have been made to publish reliable data and information, but the author and the publisher cannot assume responsibility for the validity of all materials or for the consequences of their use.

Neither this book nor any part may be reproduced or transmitted in any form or by any means, electronic or mechanical, including photocopying, microfilming, and recording, or by any information storage or retrieval system, without prior permission in writing from the publisher.

All rights reserved. Authorization to photocopy items for internal or personal use, or the personal or internal use of specific clients, may be granted by CRC Press LLC, provided that $.50 per page photocopied is paid directly to Copyright Clearance Center, 222 Rosewood Drive, Danvers, MA 01923 USA. The fee code for users of the Transactional Reporting Service is ISBN 0-8493-2389-4/02/$0.00+$1.50. The fee is subject to change without notice. For organizations that have been granted a photocopy license by the CCC, a separate system of payment has been arranged.

The consent of CRC Press LLC does not extend to copying for general distribution, for promotion, for creating new works, or for resale. Specific permission must be obtained in writing from CRC Press LLC for such copying.

Direct all inquiries to CRC Press LLC, 2000 N.W. Corporate Blvd., Boca Raton, Florida 33431.

Trademark Notice: Product or corporate names may be trademarks or registered trademarks, and are used only for identification and explanation, without intent to infringe.

Visit the CRC Press Web site at www.crcpress.com

© 2002 by CRC Press LLC

No claim to original U.S. Government works

International Standard Book Number 0-8493-2389-4
Library of Congress Card Number 2002019238
Printed in the United States of America 1 2 3 4 5 6 7 8 9 0
Printed on acid-free paper

6 Principles, Design, and Construction of a Two-Photon Laser-Scanning Microscope for *In Vitro* and *In Vivo* Brain Imaging

Philbert S. Tsai, Nozomi Nishimura,
Elizabeth J. Yoder, Earl M. Dolnick,
G. Allen White, and David Kleinfeld

CONTENTS

0-8493-2389-4/02/$0.00+$1.50

6.1 INTRODUCTION

Many biological processes of current interest occur below the surface layers of accessible tissue. Often the surface layers cannot easily be removed without adversely affecting the physiology and function of the deeper layers. A variety of imaging techniques have been developed to perform sectioning deep to the surface using optical, electrical, and magnetic contrast agents and recording methods. Two-photon laser-scanning microscopy (TPLSM) provides optically sectioned images from depths of 500 μm or more below the surface in highly scattering brain tissue.[1-3] This method is unique in that it can provide images with submicron lateral resolution and micron axial resolution on the millisecond time scale,[4] as is required for the study of many dynamic biological processes.

This chapter provides an overview of the technical considerations relevant to the design and assembly of a system for TPLSM suitable for *in vivo* as well as *in vitro* imaging. Examples of data taken with the microscope and auxiliary components are presented. Comprehensive reviews of TPLSM have previously been given by Denk and Webb and colleagues.[5-8] Previous descriptions of the *de novo* construction of a system for TPLSM have been given,[9,10] along with descriptions of the conversion of commercially available confocal microscopes.[11-14]

6.2 OVERVIEW

6.2.1 SINGLE-PHOTON ABSORPTION FOR IMAGING THROUGH WEAKLY SCATTERING PREPARATIONS

In traditional fluorescence microscopy, including confocal microscopy, fluorescent molecules that are either intrinsic to the tissue or artificially introduced are excited by a wavelength of light falling within the linear absorption spectrum of the molecule. A single photon is absorbed by the molecule and promotes it to an excited electronic state. Upon thermal equilibration and relaxation back to its ground state, the molecule will emit a photon that is shifted toward longer wavelengths with respect to the excitation light.

The probability of exciting fluorescence by the absorption of a single photon is linearly proportional to the spatial density of photons, i.e., the light intensity. The probability is therefore constant from any given axial plane, i.e., a plane taken normal to the propagation direction, regardless of the focusing of the incident beam. As one moves toward the focus of a beam, its intensity in a given axial plane increases as the power becomes distributed over a smaller cross-sectional area. At the same time, fewer fluorescent molecules in that plane are exposed to the illumination so that the lateral extent of the excitation is reduced. Thus, the total number of molecules excited in any plane is essentially a constant so that single photon absorption results in fluorescence throughout the entire axial extent of the incident beam.

6.2.1.1 Direct Imaging

Biological preparations that do not appreciably scatter or absorb the incident light, such as *in vitro* slice or cell culture, can be observed by a variety of direct imaging techniques,[15] typically with the use of a charge-coupled device (CCD) array detector. In whole-field fluorescent microscopy, the entire region of interest in the preparation is concurrently illuminated and all of the collected fluorescent light is recorded. This method has the advantage of a high rate of data collection — e.g., hundreds of frames per second with current array detectors — but suffers from the lack of optical sectioning. The fluorescence generated from planes outside the focal plane contributes in a nonuniform manner to the background level. The result is a lack of axial resolution and a lower signal-to-noise ratio than that for an image in which fluorescence from outside the focal plane is eliminated.

Axial resolution on the order of the diffraction limit may, in principle, be achieved with direct imaging methods in which light from regions outside the focal plane is systematically eliminated (Table 6.1). One method is to acquire data at multiple depths by shifting the focus above and below the object plane and then to use the images from out-of-focus planes, in conjunction with a deconvolution procedure, to model and subtract the out-of focus light.[16-18] This method and its extensions have the advantage of experimental simplicity in that only a motorized focus control needs to be added to a standard microscope. On the other hand, diffraction by the open aperture of the objective leads to a set of dark rings in the transfer function of the objective, so that this method is insensitive to the spatial frequencies of these rings. This is the so-called "missing-cone" problem in which the cone represents spatial frequencies in radial and axial momentum space (i.e., k_r and k_z).

TABLE 6.1
Nominal Properties of Techniques for Functional Imaging with Fluorescent Indicators

Mode	Technique	Axial Resolution	Lateral Resolution	Frame Period (100 by 100 pixels)	Depth Penetration
Direct Image Formation (CCD Acquisition)	Full Field	$>>\lambda$	$\cong\lambda$	~100 Hz	$\sim\Lambda_{scattering}$
	Vibrating Grating	$\sim\lambda$		<30 Hz	
	Deconvolution				
	Interferometric	$<<\lambda$			$<<\Lambda_{scattering}$
Point Scanning (PMT Acquisition)	Confocal	$\sim\lambda$		~10 Hz	$\sim\Lambda_{scattering}$
	Multiphoton Excitation			>100 Hz (resonant or AOM line scan)	$>>\Lambda_{scattering}$

An alternate procedure is to project a line grating into the object plane so that the projected image has a spacing on the order of the lateral diffraction limit. When this grating is modulated in time, only the part of the signal that emanates from the object plane is concurrently modulated. Thus, information about the intensity distribution in the object plane only may be extracted.[19,20] A final set of methods is applicable only to physically thin objects and relies on an interferometric cavity to set up an optical field that varies in the axial direction.[21-23] This may be used to achieve axial resolution on length scales of less than one wavelength.

6.2.1.2 Confocal Laser-Scanning Microscopy

Laser-scanning microscopy provides an improved means to achieve axial resolution compared with direct imaging techniques. An incoming laser beam is deflected by a pair of rotating mirrors, mounted at orthogonal angles, and subsequently focused by a microscope objective onto the preparation. The angular deflection of the collimated laser beam causes the focused spot to move across the preparation in a specified raster pattern. The fluorescent light generated at the focal volume is collected by a detector as a function of time; this time series is transformed back into a position in the preparation along the trajectory of the spot. The drawback to laser-scanning methods of microscopy is a reduced speed of acquisition compared with direct imaging techniques. The maximum acquisition rate is limited by the speed at which the scan mirrors can raster across the region of interest.

In confocal microscopy, axial resolution is obtained by preferentially collecting fluorescent light generated near the focal plane while rejecting light generated outside the focal plane. Specifically, the fluorescent light is refocused along the same beam path as the excitation light. After passing back through the scan mirrors, a process referred to as "descanning," the light is spatially filtered by a small aperture, or pinhole, whose radius is chosen so that its image in the preparation matches or exceeds the diffraction-limited radius of the illuminated region. The pinhole preferentially passes fluorescent light generated near the focal plane. Although confocal microscopy works well for optically thin preparations, it is inefficient for preparations in which substantial scattering occurs. As the fluorescent light becomes more heavily scattered, a greater portion of the photons from the focal plane are deflected from their original trajectories and thus blocked by the pinhole and remain undetected. Conversely, an increasing portion of the light from outside the focal plane will be deflected to pass through the pinhole. The result is a drop in the signal-to-noise ratio.

6.2.2 TWO-PHOTON LASER-SCANNING MICROSCOPY FOR STRONGLY SCATTERING PREPARATIONS

Two-photon laser-scanning microscopy utilizes laser light at approximately twice the wavelength of that used in traditional, one-photon microscopy. These photons carry half of the energy required to promote a molecule to its excited state, and the excitation process requires simultaneous absorption of two photons from the

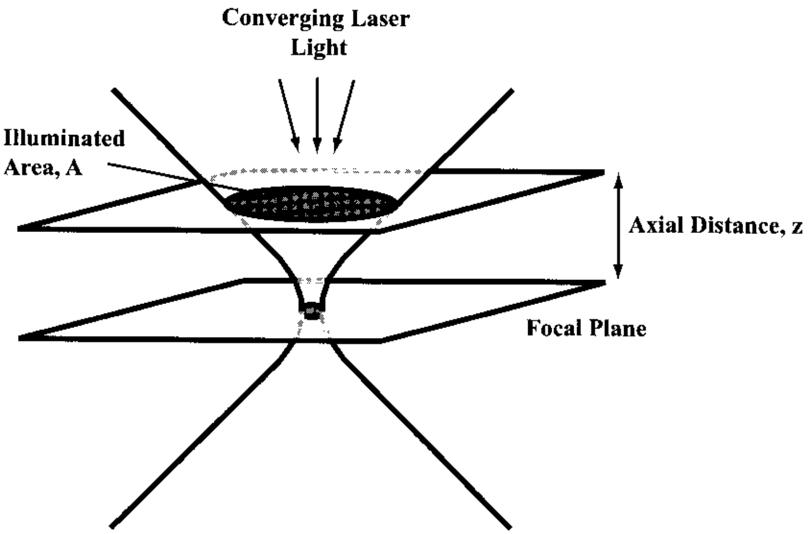

FIGURE 6.1 Cartoon of laser light near the focus of an objective. The shaded regions indicate the cross-sectional area in a given plane, normal to the direction of propagation, that is illuminated by the converging laser light. The illuminated cross-sectional area is seen to decrease as the distance to the focal plane decreases.

excitation beam. The probability of two-photon absorption thus scales with the square of the incident laser intensity. This nonlinear absorption process provides an intrinsic mechanism for optical sectioning solely by the incident beam.

As illustrated in Figure 6.1, the total fluorescence generated from a given cross-sectional plane, F_{total}, is proportional to the square of the incident intensity I and the illuminated area A. The intensity is defined as the incident laser power P divided by the illuminated area; i.e., $I = P/A$. The illuminated area in a given plane is proportional to the square of the axial distance z between that plane and the focal plane; i.e., $A \propto z^2$, at least for z larger than the confocal length, $z_{confocal}$, where

$$z_{confocal} \equiv \frac{1}{2\pi}\frac{\lambda_o}{n}\left(\frac{n}{NA}\right)^2 \tag{6.1}$$

and n is the optical index of the preparation at the excitation wavelength λ_o, NA is the numerical aperture of the objective, and the ratio (n/NA) is a purely geometric factor.[24] Thus,

$$F_{total} \propto I^2 A \propto \left(\frac{P}{z}\right)^2 \tag{6.2}$$

The amount of fluorescence generated from a given axial plane is seen to decrement as a quadratic function of the distance from the focal plane (Figure 6.2). The integrated fluorescence for $z \gtrsim z_{confocal}$ is thus finite; i.e.,

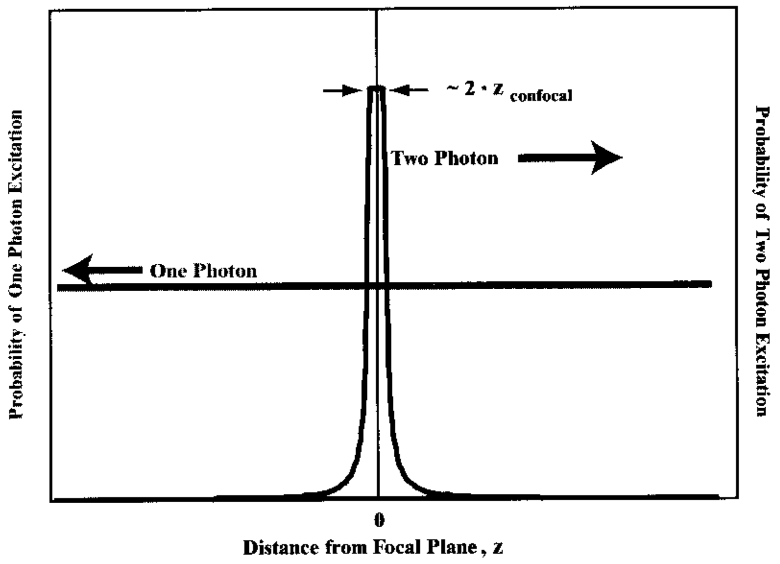

FIGURE 6.2 The integrated excitation of fluorophores within an axial plane as a function of the axial distance, z, from the focus. Single-photon excitation results in an excitation profile that is constant with axial distance (light line). Two-photon excitation results in an excitation profile that falls off quadratically with axial distance from the focal plane (dark line).

$$2\int_{z_{\text{confocal}}}^{+\infty} dz\, F_{\text{total}} \propto 2\int_{z_{\text{confocal}}}^{+\infty} dz\left(\frac{P}{z}\right)^{2} \rightarrow \text{Constant} \tag{6.3}$$

and only light within a focal depth, $z \lesssim z_{\text{confocal}}$, contributes significantly to the signal. Thus, with TPLSM, all of the fluorescent light can be collected as signal, regardless of scattering. In contrast, the same integral (Equation 6.3) diverges for single-photon absorption.

The probability of simultaneously absorbing two photons is small compared to the probability of single-photon absorption at half the wavelength. Therefore, a pulsed laser source is necessary to provide the large incident intensities required to generate significant two-photon signals while concurrently maintaining the average power at levels that avoid heating of the preparation. The use of ultrashort laser pulses, i.e., 10 to 100 fsec, allows for the greatest efficiency and depth penetration while reducing the potential for thermal damage to the preparation (but note the conclusions of Konig et al.[25]). In particular, the extent of thermal damage depends on the average power delivered by the incident beam, while the depth penetration is a function of the instantaneous peak power.

Two-photon laser-scanning microscopy is uniquely suited for optically sectioning through thick preparations.[5,6,26-29] In brief:

1. The fluorescent signal is not descanned; i.e., the fluorescent light does not require spatial filtering with a pinhole, as is the case for confocal micros-

copy. This yields a higher collection efficiency for scattering preparations. It further requires a much simpler alignment of collection optics compared to confocal microscopy.

2. The use of near-infrared light for two-photon excitation, as opposed to blue/UV light for single-photon excitation, is preferable with biological preparations. Wavelengths in the near-infrared are less heavily scattered as well as less likely to be absorbed by biological molecules. In particular, flavins and other molecules involved in bioenergetics are far less excitable by near-infrared light than by UV/blue light.
3. The two-photon spectra of fluorophores are generally broader than their one-photon counterparts and are spectrally separated further from the fluorescence emission peak. Both of these characteristics simplify the technical task of separating the excitation and emission light and allow for the simultaneous excitation of multiple dyes with a single laser source.

6.3 BASICS

6.3.1 RESOLUTION

The fundamental axial length scale is the confocal length (Equation 6.1), $z_{confocal}$. The axial resolution or depth of focus, denoted δz, is proportional to $z_{confocal}$. A worst-case estimate for δz is when the intensity goes through a first zero along the optical axis, which occurs for[24]

$$\delta z = 4 \cdot \pi \cdot z_{confocal} = 2\frac{\lambda_o}{n}\left(\frac{n}{NA}\right)^2 \tag{6.4}$$

where λ_o/n is the wavelength in the preparation. An analogous expression holds for the lateral resolution, denoted δr. A worst-case estimate for δr is when the intensity goes through a first zero along a radius in the focal plane, which occurs for[24]

$$\delta r = 1.2 \cdot \pi \frac{NA}{n} z_{confocal} = 0.6\frac{\lambda_o}{n}\left(\frac{n}{NA}\right) \tag{6.5}$$

For the practical case of a 40× magnification water immersion lens with NA = 0.8, the confocal length for 800-nm light is $z_{confocal} \cong 0.25\ \mu m$, for which $\delta z = 3\ \mu m$ and $\delta r = 0.6\ \mu m$.

6.3.2 SCATTERING BY BRAIN TISSUE

The beam will maintain a focus as long as the elastic scattering length, denoted $\Lambda_{scatter}$, is much greater than the depth of focus, i.e., for

$$\Lambda_{scatter} >> z_{confocal}$$

The scattering length corresponds to the length over which the incident light remains essentially undeflected. For neocortex in living rat, $\Lambda_{scatter} \sim 200$ μm,[27,29,30] so that the depth penetration of TPLSM is limited only by the available power. However, for some preparations, such as the granule cell layer in mouse cerebellum, the interpretation of preliminary data (Denk and Kleinfeld, unpublished) suggests that $\Lambda_{scatter} \sim z_{confocal}$ and TPLSM is no longer effective.

6.3.3 PHOTOBLEACHING AND PHOTODAMAGE

The nonlinear excitation profile of TPLSM results in localization of any photodamage, related to bleaching of the fluorophore or otherwise, that may occur. In contrast, single-photon excitation results in photodamage throughout the entire axial extent of the beam. Further, for both single- and two-photon imaging techniques, the incident beam can induce heating of the nervous tissue, although this effect may be substantial only when the average incident power exceeds ~0.1 W for the near-infrared wavelengths involved in TPLSM.[31]

Increased photobleaching at the focus, possibly driven by third-order or higher nonlinear processes, is a possibility with two- vs. single-photon excitation. Some experimenters have observed photobleaching rates that always scale linearly with two-photon absorption[25,32] or scale supralinearly with absorption only at relatively high intensities,[33] while other experimenters have observed the supralinear relation at all intensities.[34,35] At extremely high peak powers unlikely to be achieved under normal imaging conditions, the intensity of the laser pulse at the focus can cause ionization and result in permanent damage to the preparation.

For imaging through optically thick preparations, TPLSM offers fundamental advantages over single-photon excitation microscopy. For thin preparations, the possibility of increased but localized photodamage leaves the choice between the single- and two-photon methods unresolved.

6.3.4 LIGHT SOURCE

Pulsed laser light is not monochromatic. A temporally short pulse comprises a correspondingly broad range of wavelengths. While the exact width will depend on the precise shape of the pulse, the spectral width, $\Delta\lambda$, must scale with the temporal width, τ_P, as

$$\Delta\lambda \sim \frac{\lambda_o^2}{c\tau_P} \tag{6.6}$$

where λ_o is the center wavelength. For a sufficiently short pulse, the spectral width of the pulse can extend beyond that of the two-photon excitation spectrum for a given fluorescent molecule. In this limit, the excitation efficiency for an excessively short pulse can be lower than that for a longer pulse.

A laser with an appropriate pulse width as well as center wavelength, typically between 730 and 1000 nm, must be used in a TPLSM system (see Siegman[36] for a general review of lasers). Ti:Sapphire-based laser systems have been reported to produce pulses with widths shorter than 10 fsec, while commercially available Ti:Sapphire systems capable of generating roughly 100-fsec-duration pulses are readily available and are used for our system (Section 6.4). The pulse is broadened to 200 fsec or more at the exit of the objective. The corresponding full spectral bandwidth is ~10 nm. This width is less than the width of the two-photon absorption band of many relevant dyes, e.g., 80 nm for fluorescein.

The fluorescent light generated by TPLSM is sensitive to fluctuations in the laser power, the center wavelength of the pulse, and the spectral width of the pulse. Pulses with different spectral densities may be characterized by the same width yet provide different peak powers and thus different excitation strengths,[37] as demonstrated by the examples of Figure 6.3. On the one hand, the efficiency of two-photon excited fluorescence increases with increasing spectral width, i.e., as $\Delta\lambda$, or equivalently increases inversely with decreasing pulse width, i.e., as τ_p^{-1} (Equation 6.6). Thus, efficient pulses are associated with a large spectral bandwidth. On the other hand, a high level of spectral dispersion in the objective may lead to a drop in spatial resolution. This occurs when the optical index of the glasses in the objective significantly varies as a function of wavelength, although it is typically a small effect for the near-infrared wavelengths and 100- to 200-fsec pulse widths used in TPLSM.[38]

The spectral components of the pulse can be nonuniformly distributed through the pulse — a condition referred to as chirp — so that there is a systematic shift in frequency between the start and end of a pulse (Figure 6.3c). Under ideal conditions the chirp of the laser pulse should be zero at the focus of the objective so that the spectral composition of the pulse is uniform across the pulse. This results in a minimum pulse width and is usually achieved with external compensation for the group dispersion of the pulse.[39]

The average output power of the laser can be monitored with a simple photodiode. The center wavelength and the spectral width of the pulse of the laser can be determined with a basic spectrometer. While a fast oscilloscope can be used to display the repetition rate of the laser, even the fastest available oscilloscopes are currently unable to measure the laser pulse width directly. However, an interferometric autocorrelator can be built to monitor the shape of the pulse (Appendix B). The temporal distribution of wavelengths can be directly detected only by phase measurements, using a frequency-resolved optical gating or related technique.[40]

6.3.5 DELIVERY OF LASER LIGHT

The output parameters of a commercial laser system are unlikely to match the requirements of the microscope perfectly. The output beam may not be optimally collimated or may be collimated with a beam diameter too small or too large for use in the microscope. To compensate, the beam profile is calculated along the direction of propagation and can be reshaped using either lenses or curved mirrors.

6.3.5.1 Laser Beam Profile

The laser beam diameter and divergence can be calculated using the paraxial approximation, i.e., under the assumption that the intensity along the direction of propa-

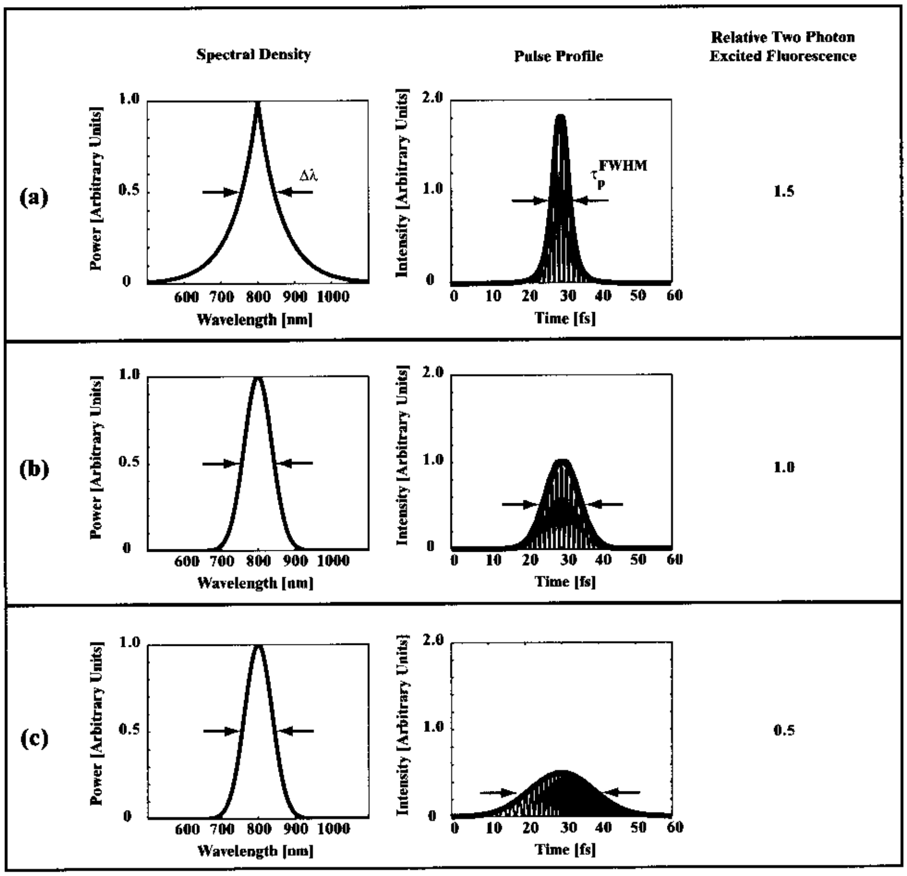

FIGURE 6.3 Pulses with different characteristics can have the same full-width half-maximal spectral width, indicated by $\Delta\lambda$. (a) A pulse with an exponential spectral envelope and the corresponding Lorentian pulse shape with a full-width half-maximal pulse width of τ_p^{FWHM}. (b) A pulse with a Gaussian spectral envelope and the corresponding Gaussian pulse shape. (c) A pulse in which the constituent frequency components are nonuniformly distributed, i.e., chirped. The extent of the chirp has been grossly exaggerated from typical conditions. Note that, for illustrative purposes, the pulse widths are about 10× shorter than those used in typical TPLSM experiments.

gation varies slowly on the scale of the wavelength, and the further assumption that the profile of the intensity follows a Gaussian distribution along the direction transverse to that of propagation.[41] This is depicted in Figure 6.4 for a divergent laser output that is refocused with an f = +500-mm lens; the beam diameter is denoted by D_{beam} and equals the diameter across the points where the intensity falls by a factor of e^{-1}. Superimposed on the Gaussian beam calculation is the calculation for the same system in the geometric optics limit. The result demonstrates that, with the exception of regions close to a focus, the Gaussian beam calculation can be approximated by a geometric optics calculation with modest accuracy.

the same system in the geometric optics limit. The result demonstrates that, with the exception of regions close to a focus, the Gaussian beam calculation can be approximated by a geometric optics calculation with modest accuracy.

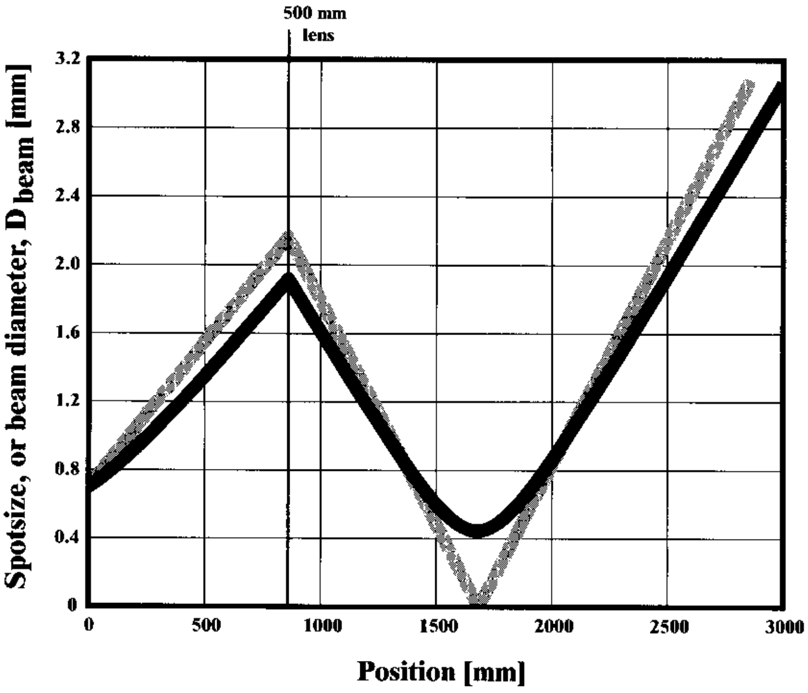

FIGURE 6.4 Calculations of the laser beam diameter, D_{beam}, as a function of distance for a beam with a starting diameter of D_{beam} = 0.70 mm and a divergence of 1.7 mrad. These values are typical for the output of a Ti:Sapphire laser. An f = +500-mm lens is placed 860 mm from the laser output aperture. The calculation for a Gaussian beam is shown as the dark line, while the geometric optics limit is depicted as the light line.

6.3.5.2 Reshaping the Laser Beam

Several different methods are available to change the divergence and diameter of a laser beam, as depicted in Figure 6.5. Lenses are simple to align, yet, as a general consideration, the glass will introduce an additional source of pulse dispersion (Figures 6.5a and 6.5b). Their effect on a 100-fsec pulse is small; thus, lenses may be used with commercial Ti:Sapphire systems, but lenses may introduce substantial dispersion for shorter, i.e., ~10-fsec, pulses. Curved metal mirrors do not introduce dispersion, yet they must be used off axis and thus introduce astigmatism into the laser beam. Specifically, for a two-curved-mirror telescope, typically sized mirrors must used substantially off axis to allow the beam to reflect from their centers yet pass the edge of the companion mirror (Figure 6.5c). The resulting astigmatism may degrade the sharpness of the laser focus at the preparation. A single-mirror scheme is a simple yet viable means to change the size of the beam (Figure 6.5d).

The technical characteristics involved with several telescope designs are:

1. A pair of achromatic doublets can be used as a Keplerian telescope (Figure 6.5b). The lens separation should be approximately the sum of the two

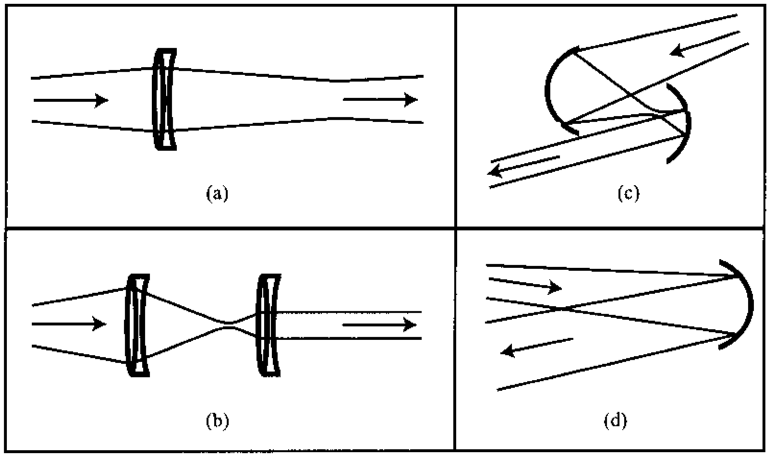

FIGURE 6.5 Four possible methods for reshaping a laser beam: (a) a single, long focal length lens, as used for the calculation of Figure 6.4; (b) a Keplerian telescope; (c) a telescope constructed with two curved mirrors; (d) a single, long focal length curved mirror.

focal lengths, but the actual location of the telescope along the beam path is flexible. The telescope can easily be adapted to provide different magnifications by choosing different combinations of lenses at the appropriate separation. The disadvantages of this configuration include the need for rails or precision translation stages for precise alignment and the dispersion produced by the lenses.

2. A curved-mirror telescope can be used with the mirror separation approximately equal to the sum of the two focal lengths (Figure 6.5c). In this Keplerian telescope, the actual location of the curved-mirror telescope is flexible, and the telescope can be adapted to provide different magnifications with the choice of different combinations of curved mirrors. This configuration also requires rails or precision translation stages for precise alignment. No dispersion is added to the system by the mirrors, but astigmatism is introduced into the laser pulse because the mirrors are used at substantially off-axis angles.
3. A single-focal length achromatic doublet can be used to reshape the beam (Figure 6.5a). An achromatic doublet is placed approximately one focal length from the original focus of the laser, which is typically inside the laser cavity. Although the alignment of a single lens is simplified compared to multielement configurations, the collimated beam diameter and placement of the lens are completely determined by the focal length of the lens. As with all lenses, some dispersion is added to the system by this configuration.
4. A single, long focal length curved mirror can be used to reshape the beam (Figure 6.5d). The lens is placed approximately one focal length from the original focus of the laser, which typically is inside the laser cavity. Alignment of the mirror is simplified compared to multielement

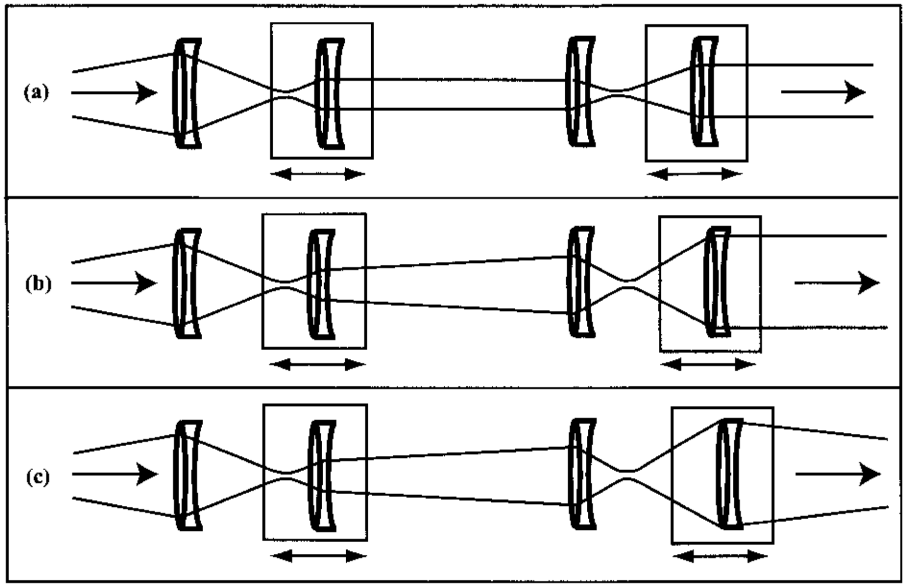

FIGURE 6.6 Ray diagrams for a dual telescope system with four lenses. The output beam diameter and divergence can be completely controlled by translating two of the four lenses. For illustration, we take the input beam to be divergent. (a) A collimated, smaller diameter output; (b) a collimated, larger diameter output; (c) a converging, larger diameter output.

configurations, but the collimated beam diameter and mirror placement are completely determined by the focal length of the mirror. Although no dispersion is added to the system by the mirror, a slight astigmatism is introduced into the laser pulse because the incoming and outgoing beams are off axis only in one plane.

5. For complete control of the beam profile with a fixed set of achromatic doublets or mirrors, a four-element, double-telescope system should be implemented (Figure 6.6). The laser beam diameter and the divergence can be altered by adjusting the location of two of the four elements. The deficit of this system is additional dispersion. Note that, in principle, a three-element system provides sufficient degrees of freedom but is somewhat more difficult to adjust.

In general, the laser beam should be collimated to minimize the spherical aberrations of the objective. As a practical matter, it may be necessary to introduce a slight convergence or divergence to the beam, as most lenses are designed to minimize spherical aberrations for visible (400 to 600 nm) light rather than near-infrared (700 to 1000 nm) light. The final size of the beam represents a compromise between resolution, which increases as the back aperture of the objective is increasingly filled, and throughput, which is maximal when the back aperture is underfilled. This tradeoff is illustrated in Figure 6.7 in terms of the normalized beam diameter, D_{beam}/D_{BA}, where D_{BA} is the diameter of the back aperture of the objective.

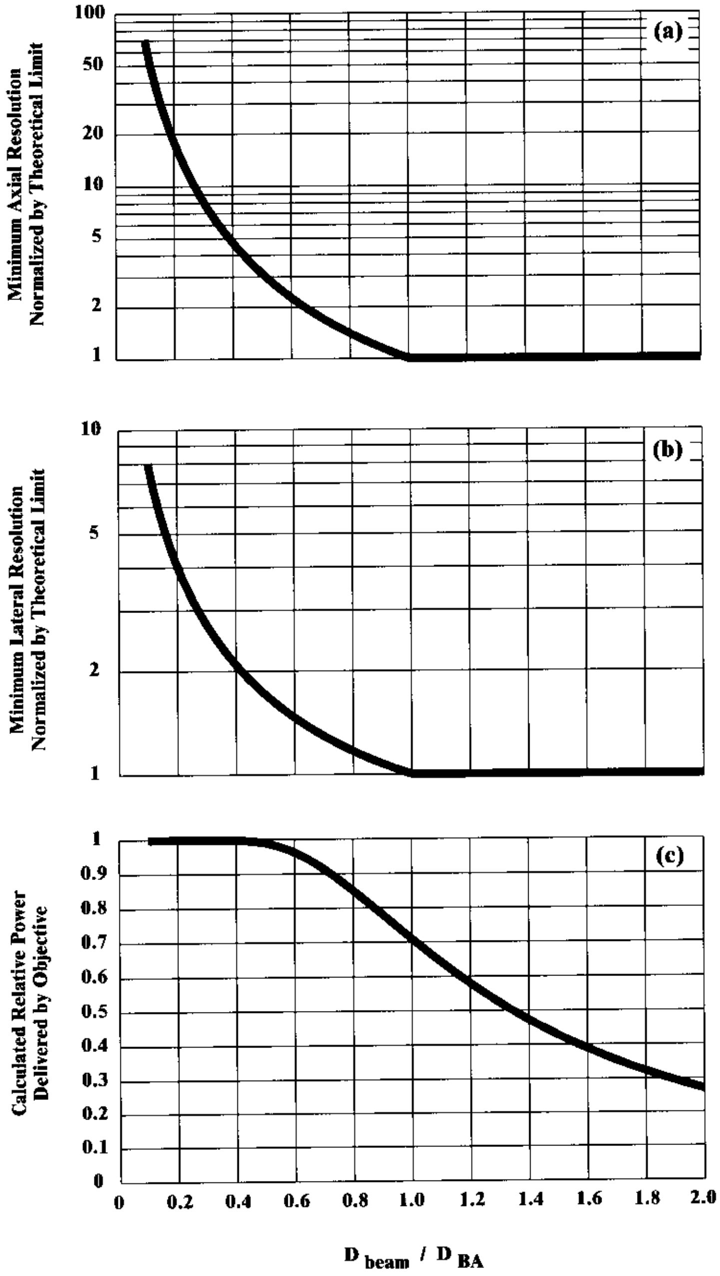

FIGURE 6.7 The tradeoff between power throughput and optical resolution as a function of the size of an incident Gaussian beam, normalized in terms of the filling factor D_{beam}/D_{BA}. The resolution was estimated in the plane wave limit, while the power was calculated in the Gaussian limit. (a) Lateral resolution vs. normalized radius; (b) axial resolution vs. normalized radius; (c) relative power vs. normalized radius.

6.3.6 DESIGN OF A SCAN SYSTEM

We consider in detail the manipulation of the path of the laser beam as a means to scan a focused spot across the preparation. The essential idea is that the objective converts the incident angle of a collimated beam into the position of a diffraction limited spot on the focal plane (Figure 6.8a). The focused laser spot can be moved across a stationary preparation by changing the angle of the incident beam. In order to change the angle without physically moving the source, one uses a system of mirrors and auxiliary lenses according to one of two schemes.[42] The first method involves a standard 160 mm tube length objective, i.e., a lens optimized for an image plane at 160 mm from the rear focal plane of the objective, in conjunction with a rotating mirror and a scan lens to deflect the rotated light back into the beam path (Figure 6.8b). A disadvantage to this configuration for TPLSM is that the incoming light to the objective is convergent rather than parallel. This can lead to astigmatism in the focused beam if a dichroic mirror, used for the collection of emitted light, is placed directly behind the objective.[5]

An alternative scheme for the scan system is to use an infinity-corrected objective, together with a rotating mirror and a tube lens as well as a scan lens (Figure 6.8c). In this configuration, the two auxiliary lenses serve to translate the angular deflection of the mirror into an incident angle at the objective while allowing the input to the mirror and the input to the objective to be collimated. This is the configuration used in our system, which will now be described in greater detail (Figure 6.9). The relevant variables are

f_1 ≡ Focal length of scan lens
f_2 ≡ Focal length of tube lens
d_1 ≡ Distance between the scan mirror pivot point and the scan lens
d_2 ≡ Distance between the scan lens and the tube lens
d_3 ≡ Distance between the tube lens and the back aperture of the objective
D_{SM} ≡ Effective diameter of the scan mirror
D_{BA} ≡ Diameter of the back aperture of the objective
D_{beam} ≡ Diameter of the beam at the back aperture
d_{SM} ≡ Distance between a pair of scan mirrors

The issue of one- vs. two-dimensional scanning can be separated from the issue of constraining the optics in the beam path. Thus, for clarity, we focus first on a one-dimensional scan system.

6.3.6.1 Constraints on Axial Distances and Optical Apertures

We consider the optimal alignment and layout of optics, with reference to Figure 6.9. The constraints are:

1. Infinity-corrected objectives require the incident light to be collimated at the back aperture of the objective. If the input to the scan system is a collimated laser beam, then the scan lens and tube lens must be configured as a telescope. Therefore, their separation is given by

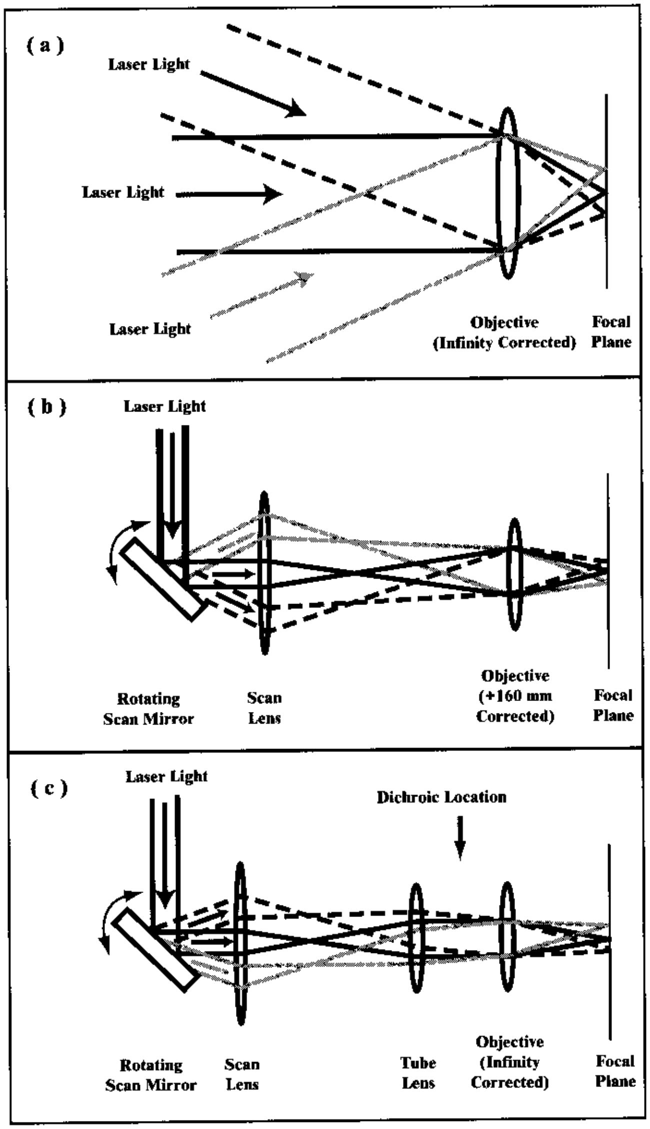

FIGURE 6.8 Illustration of different configurations for laser scanning. (a) A scanning system with only an objective. The collimated laser source must be physically moved and rotated behind an infinity-corrected objective. (b) A scanning system with a single intermediate lens, i.e., the scan lens, in addition to the objective. The objective is taken as optimized for a 160 mm image distance. The rotating mirror is imaged onto the back aperture of the objective. Note that the light is convergent behind the objective. (c) A scanning system with two intermediate lenses, i.e., the scan lens and the tube lens, in addition to the objective. The objective is taken as optimized for an infinite image distance. A scan lens and tube lens are placed between a rotating scan mirror and an infinity-corrected objective. The mirror surface is imaged onto the back aperture of the objective, and the light between the objective and the tube lens is collimated and thus suitable for the placement of a dichroic mirror.

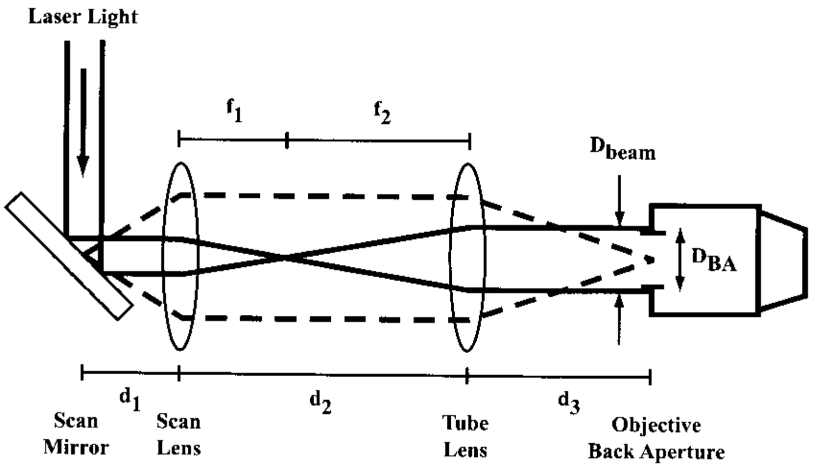

FIGURE 6.9 The alignment of optics in a scanning system consisting of an objective, tube lens, and scan lens. The actual laser pathway is indicated by the solid lines. The dashed lines depict the imaging condition between the center of the scan mirror and the center of the back aperture of the objective. The laser path is magnified to just overfill the back aperture, and the imaging condition (see text) prevents motion of the laser spot at the back aperture as the laser beam is scanned.

$$d_2 = f_1 + f_2 \tag{6.7}$$

2. The pivot point of the scan mirror should be imaged to the center of the back aperture of the objective to minimize motion (spatial deviations) of the laser path at the back aperture plane. This imaging condition is satisfied by

$$d_1 = \frac{(f_1)^2}{f_2} + f_1 - d_3\left(\frac{f_1}{f_2}\right)^2 \tag{6.8}$$

   This condition serves to maintain constant laser power through the back aperture of the objective as the scan mirror is rotated. A graph of the required separation d_1 as a function of the separation d_2 for six different choices of scan lens focal lengths and a tube lens with a focal length of $f_2 = +160$ mm is shown in Figure 6.10.
3. The incident laser beam should slightly overfill the back aperture of the objective in order to utilize its full NA; i.e.,

$$D_{beam} > D_{BA} \tag{6.9}$$

   This generates the highest resolution for a given objective.

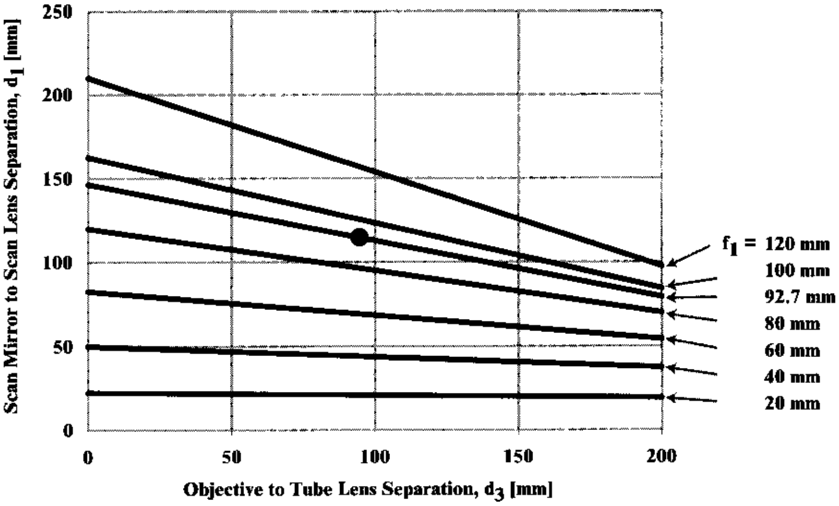

FIGURE 6.10 The calculated scan mirror to scan lens separation distance, d_1, as a function of the objective to tube lens separation distance, d_3. The calculation is shown for several choices of scan lens focal lengths, f_1. The focal length of the tube lens is assumed to be $f_2 = +160$ mm. The dot marks the actual values, $d_3 = 95$ mm and $f_1 = +92.7$ mm, used in our system.

4. Typical scan mirrors are only a few millimeters in dimension. The simultaneous requirements that the beam should underfill the scan mirrors as a means to avoid losses due to diffraction, yet slightly overfill the back aperture of the objective as a means to maximize the spatial resolution at the focus, constitutes a magnification constraint on the scan system. The required magnification, denoted m, is given by

$$|m| \equiv \frac{D_{BA}}{D_{SM}} \cong 2 \text{ to } 4 \tag{6.10}$$

where the numerical values are appropriate for typical dimensions of objectives' back apertures and scan mirrors. For the case in which a standard $f_2 = +160$-mm tube lens is used in the scan system, the required focal length of the scan lens is determined by a second constraint on the magnification; i.e.,

$$f_1 \equiv \frac{f_2}{|m|} \cong 40 \text{ to } 80 \text{ mm} \tag{6.11}$$

5. The above constraints (Equations 6.7 to 6.11) reduce the scan system to a single degree of freedom. For a given separation distance between the tube lens and the objective d_3, the imaging constraint determines the scan

5. The above constraints (Equations 6.7 to 6.11) reduce the scan system to a single degree of freedom. For a given separation distance between the tube lens and the objective d_3, the imaging constraint determines the scan

> lens–to–scan mirror separation d_l or vice versa (Figure 6.10). In practice, many objectives are designed to be corrected for chromatic aberration at a fixed value of d_3. By convention, this is taken to be
>
> $$d_3 \cong 95 \text{ mm} \tag{6.12}$$
>
> This constraint will further increase the collection efficiency of the tube lens for visual inspection of the preparation. In practice, d_3 is also constrained by the physical size of the detector assembly.

The scan lens should be a lens with a small f-number, i.e., ratio of focal length to clear aperture, that is well corrected for spherical, chromatic, and off-axis aberrations. A minimal scan lens could be an achromatic doublet with an f-number of 2. More precise scan lenses are available from specialized manufacturers and are particularly valuable for applications involving large scan angles. In practice, stereoscope objectives are well corrected for off-axis aberrations and work well as scan lenses, as discussed in Section 6.4.

6.3.6.2 Two-Dimensional Scanning

A true, distortion-free, two-dimensional scan can be obtained with two scan mirrors and the use of additional optics between the scan mirrors to insure that the centers of both mirrors and the objective back aperture are all conjugate planes of one another. The addition of intermediary optics, while conceptually straightforward and employed in commercial instruments, e.g., the Biorad MRC series, makes proper alignment more difficult and can result in additional dispersion or astigmatism.

A simpler two-dimensional scan configuration can be used that utilizes no intermediary optics if the separation between the scan mirrors can be made small compared to focal length of the scan lens; i.e.,

$$f_l >> d_{SM} \tag{6.13}$$

The conjugate plane of the back aperture is placed halfway between the two scan mirrors. The small deviation from the exact imaging conditions results principally in two effects. The first is a slightly increased sensitivity of the focused beam profile to defects on the scan mirrors. The second is a slight lateral motion of the beam at the back aperture of the objective while the beam is scanned. This motion results in increased clipping, i.e., vignetting, of the beam at larger scan angles. The excitation intensity will therefore be lower at the edges of the scan than at its center (Figure 6.11).

The focal length of the scan lens is constrained from above by the requirement of sufficient magnification (Equation 6.11). For a tube lens with a focal length of $f_2 = +160$ mm, we have $f_l = |m|^{-1} f_2 \approx 80$ mm. As a compromise, our system (Section 6.4) uses a scan lens of focal length $f_l = +92.7$ mm. This distance is large compared to the spacing between the two scan mirrors in our system, i.e., $d_{SM} = 7.6$ mm, but

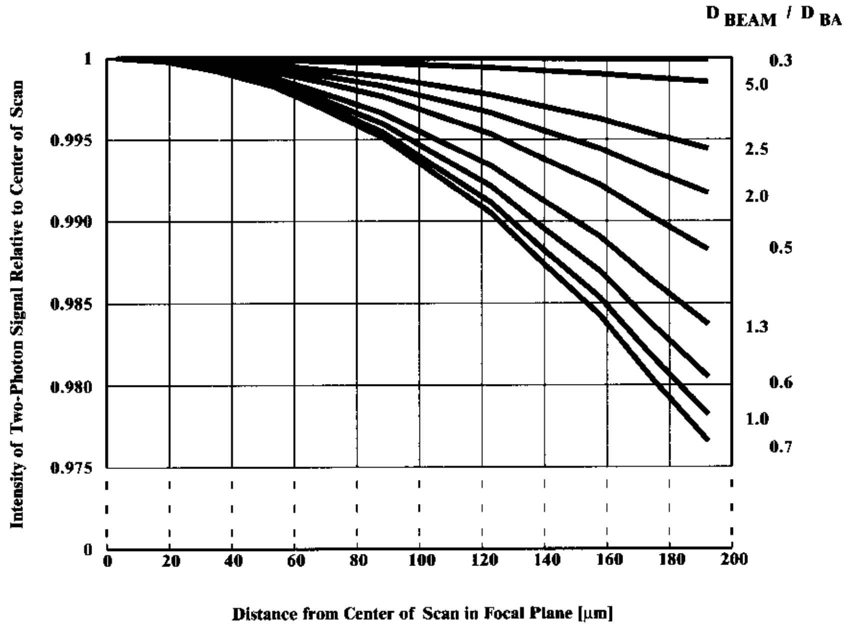

FIGURE 6.11 Theoretical calculation of the spatial inhomogeneity of the squared power, which corresponds to the two-photon excitation rate, due to the lateral motion of the scanned laser spot at the back aperture of the objective. The calculation was carried out in the geometric optics limit with the assumption of a Gaussian transverse beam profile. The different curves correspond to filling factors D_{beam}/D_{BA}. All parameters as specified in Section 6.4.

slightly larger than the constraint in Equation 6.11, so that we slightly underfill the back aperture. A typical imaging experiment utilizes a 40× magnification objective with a back aperture of $D_{BA} = 8$ mm. The theoretical two-photon intensity profile for different filling rations D_{beam}/D_{BA} is estimated by modeling this system with geometric optics (Figure 6.11). The calculated intensity deviations due to motion of the laser path at the objective back aperture plane are seen to be small for typical scanning conditions.

6.3.7 FLUORESCENT LIGHT DETECTION

The fluorescent signal generated in the illuminated region of the preparation is incoherent and emitted over the entire 4π solid angle. A portion of the signal is collected in the backward direction by the objective and deflected by a dichroic beamsplitting mirror and focused onto a photomultiplier tube (PMT) (Figure 6.12). Filters and additional dichroic mirrors and detectors can be used to further isolate the fluorescent signal and, if required, separate different fluorescent signals according to wavelength. For preparations that are not too optically thick, e.g., slice or cell culture, an additional detector can be placed beneath the preparation to collect the signal emitted in the forward direction[43] (Figure 6.12).

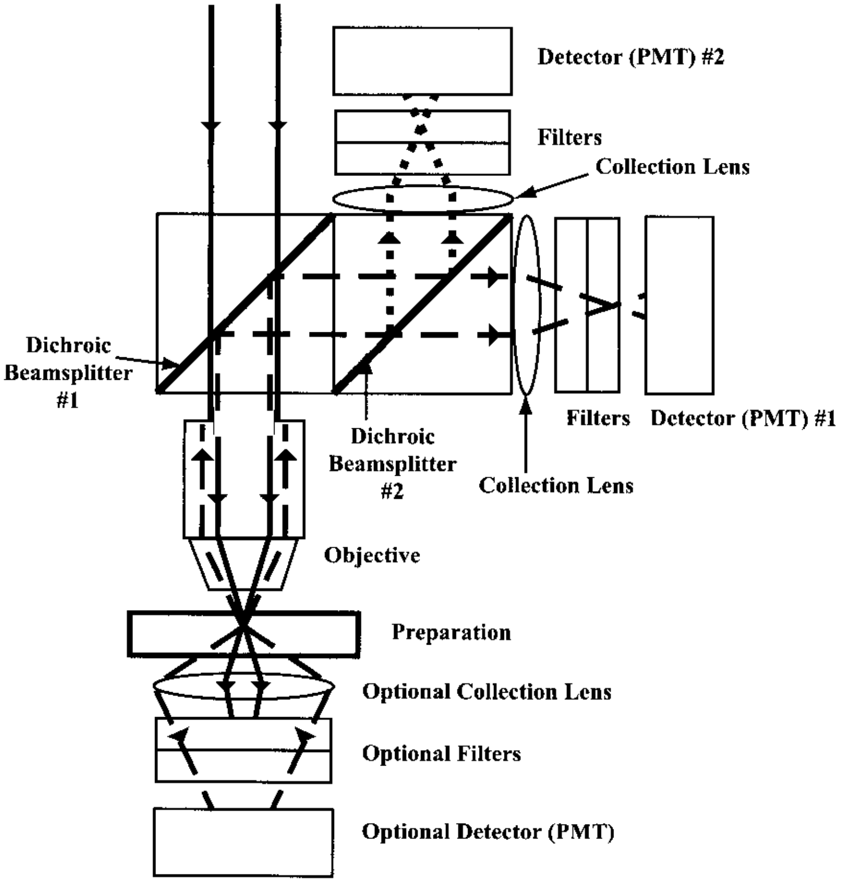

FIGURE 6.12 Schematic of the detection configuration for two-photon excited fluorescence. The excitation laser light is depicted as a solid line, while the fluorescent signals are shown as dashed and dotted lines. The collection system shown below the sample stage can be added for preparations, such as brain slice, that are not too optically thick.

6.3.7.1 Placement of Detector Assembly

The detector assembly should be placed directly above the objective. The two main considerations in this choice of detector position are:

1. Collection efficiency is increased by placing the collection assembly directly above the objective. Although light emitted from the focal plane of the infinity-corrected objective should ideally be collimated as it returns through the back aperture, the actual fluorescence will diverge due to scattering and diffraction. In particular, it is mainly the scattered light that will miss the clear aperture of the tube lens. The unscattered light collected by the objective will almost exactly retrace the beam path of the excitation laser. Therefore, placing the detector assembly as close to

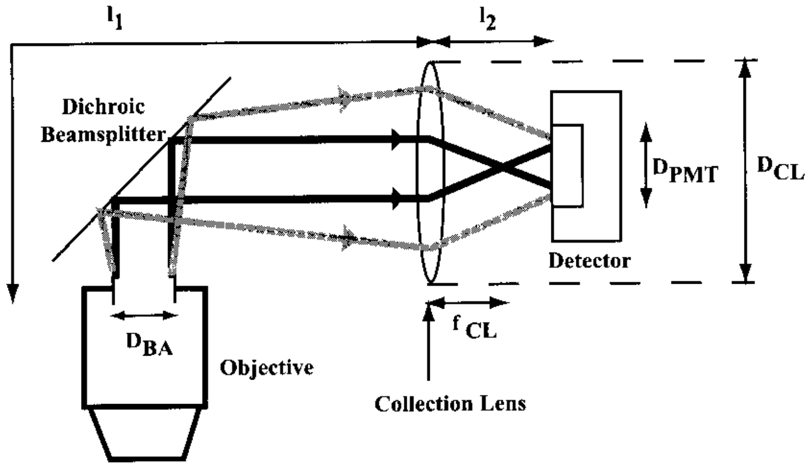

FIGURE 6.13 Placement and separations of detector elements for two-photon excited fluorescence. Unscattered fluorescent light is depicted as a dark line, while scattered fluorescent light is depicted as a gray line.

the objective as possible should result in improvements for more strongly scattering preparations.

2. Fluorescent light collected from an infinity-corrected objective will be nearly collimated just above the objective. Placing the dichroic mirror in the path at this point, rather than at a location where the beam is diverging, reduces the sensitivity of the signal to local defects on the dichroic mirror.

6.3.7.2 Constraints for Detection Elements

The backward collection pathway is shown in Figure 6.13 with the second dichroic mirror and PMT pathway eliminated for clarity. We note the following definitions:

l_1 ≡ Distance between collection lens and back aperture of the objective
l_2 ≡ Distance between active surface of the detector and collection lens
D_{PMT} ≡ Effective diameter of the detector active surface
f_{CL} ≡ Focal length of the collection lens
D_{CL} ≡ Clear aperture of the collection lens

The following conditions should be maintained for the choice and placement of collection optics:

1. The back aperture of the objective should be imaged onto the active surface of the PMT to minimize motion of the fluorescent signal on the detection surface. This imaging condition is given by

$$l_2 = \frac{l_1 f_{CL}}{l_1 - f_{CL}} \tag{6.14}$$

and is graphed in Figure 6.14 for five choices of collection lens focal lengths, f_{CL}.

2. The collection lens should have a large clear aperture to maximize collection of scattered light, some of which diverges as it exits the back aperture of the objective. In practice, physical constraints of the detector assembly (described in detail later) limit the clear aperture to

$$D_{CL} \approx 30 \text{ mm} \tag{6.15}$$

3. The separation between the collection lens and the objective should be minimized to within physical constraints. This also serves to increase the collection efficiency of the scattered light. As a maximal limit, we arbitrarily choose a distance at which a clear aperture is at least half of the empirically determined maximal divergent spot size from the back of a typical objective. For example, this corresponds to a half-angle spread of 11.3° from the D_{BA} = 8-mm back aperture of a 40× magnification objective. For a collection lens with a clear aperture of D_{CL} = 30 mm, this implies a spacing of

$$l_1 \cong 130 \text{ mm} \tag{6.16}$$

4. The focal length of the collection lens should be as short as possible. This, in combination with the imaging constraint of Equation 6.14, assures that

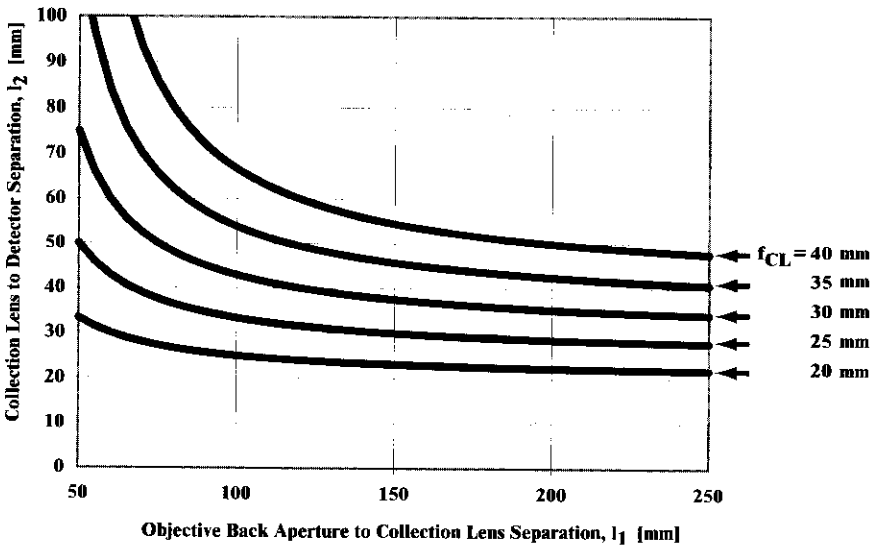

FIGURE 6.14 Graph of the imaging constraint for the distance between the collection lens and the detector, l_2, vs. the distance between the detector and the back aperture of the objective, l_1, for five choices of focal length for the collection lens.

the image of the back aperture is minified to fit onto the smaller active area of the PMT. The magnification is given by

$$|m| = \frac{f_{CL}}{l_1 - f_{CL}} \tag{6.17}$$

The active area of the PMT described in this chapter is 4 mm. The objective back apertures range up to 12 mm in diameter. Therefore, the magnification requirement for the described system is $|m| = 1/3$. Together with $l_1 = 130$ mm (Equation 6.17), we have

$$f_{CL} = 32.5 \text{ mm} \tag{6.18}$$

In many imaging applications, aberrations and misalignment of optical elements distort the spatial distribution of the collected light. This directly affects the resolution of the final image. In laser-scanning microscopy, the final image is produced as a time series of collected light intensities. All of the light collected during a given time interval contributes equally to the intensity value of the corresponding spatial pixel, at least insofar as the efficiency of the detector is spatially uniform. Thus, it is more important to collect a consistently large portion of the fluorescent light at the detector than to minimize aberrations in the collection optics.

For completeness, we note that an alternate detection system could be used in which the collected light must pass through two lenses on its way to the detector. The collection optics would then be placed in a configuration similar to that described for the scanning system. The main advantage to this configuration is that the unscattered light, which constitutes the predominant part of the signal in weakly scattering preparations, arrives at the detector as a collimated beam rather than as a focused spot. This would reduce the sensitivity of the signal to any spatial inhomogeneities in the responsivity of the active surface of the detector. The two-lens collection system suffers from the disadvantage of increased complexity and increased loss, as each added optical element produces additional reflection and diffraction.

6.4 REALIZATION

6.4.1 OPTICAL AND MECHANICAL

Our system is laid out on a 4 × 8 × 1 ft air table, which provides room for the lasers, ancillary optics, an interferometric autocorrelator, a two-photon spectrometer, and two experimental setups (Figure 6.15). Room for dispersion compensation optics, should they be required, is also available. Wherever possible, standard, commercially available optics and electronics are used to maximize the reproducibility of the system; these are summarized in Appendix A. Various adapters are fabricated to combine parts of noncompatible design. Machine drawings of these adapters are available by contacting the senior author. Lastly, ancillary electronics are supported by a hanging shelf above the air table.

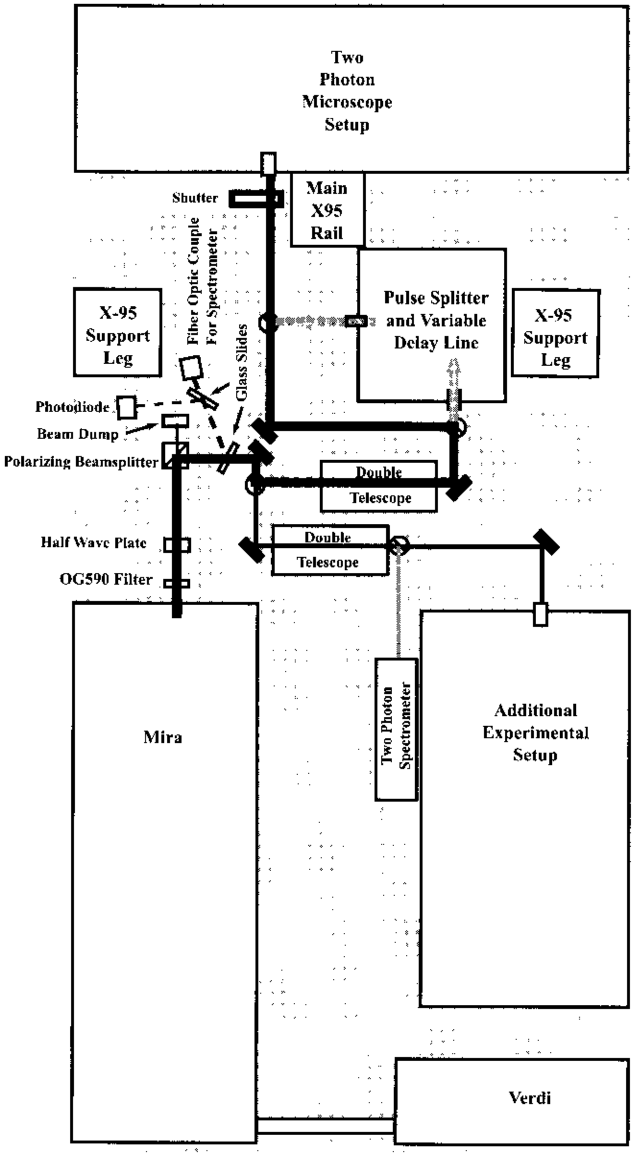

FIGURE 6.15 Schematic diagram, drawn approximately to scale, of the layout on an optical table for delivery of laser light to our two-photon laser-scanning microscope. The main beam path is depicted by the thick dark line. The beam path through the pulse splitter and delay line, used for the optical autocorrelator, is depicted by the thick gray lines. The beam path to the additional experimental setup is depicted by the thin dark line. The beam path to the two-photon spectrometer is depicted by the thin gray line. The dashed lines represent a small fraction (~4%) of the beam that is picked off with glass slides and used to monitor the output power and wavelength of the laser. Circles with diagonal lines represent protected silver mirrors in flipper mounts. Solid rectangles at 45° represent protected silver mirrors in standard mirror mounts. The dimensions of the table are 4 by 8 feet.

6.4.2 LASER SYSTEM

Our laser system consists of an Nd:Vanadate diode pump laser (Coherent Verdi V10) and a Ti:Sapphire laser (Coherent Mira 900) equipped with a broadband mirror set. Some of the important characteristics of this laser system are:

1. The diode pump laser delivers up to 10 W of pump power at a wavelength of $\lambda = 532$ nm, close to the approximately 15 W maximum thermal limit of the Ti:Sapphire crystal.
2. The Ti:Sapphire laser delivers 100- to 300-fsec pulses, at the preparation, that are tunable over the wavelength range of $\lambda_o = 700$ to 990 nm.
3. These pulses are delivered at a repetition rate of 76 MHz. Therefore, the time between the pulses is ~13 ns, which is long compared with typical fluorescent lifetimes of 1 to 10 ns.
4. The maximum average output power of the laser is approximately 1.5 W at $\lambda_o = 800$ nm, or upwards of 100× the saturation power for typical dyes.[5] This allows for more than two orders of magnitude of loss due to scattering as one probes deep into brain tissue.

Additional equipment required for laser operation include two chillers, typically supplied with the lasers, and a dry nitrogen gas purge to facilitate laser operation for wavelengths longer than 900 nm. In addition, various diagnostic equipment is essential, including an optical spectrometer, an ~500-MHz oscilloscope, an infrared view scope, and infrared view cards.

6.4.3 PATH FROM LASER TO MICROSCOPE

The delivery pathway of the laser light from the source to the scanners is depicted in Figure 6.15. A colored glass filter, type OG590, is placed immediately after the laser output port as a means to attenuate any residual $\lambda = 532$-nm pump light along the beam path. The output of the Ti:Sapphire laser is horizontally polarized; thus, the intensity of the laser output may be controlled by manipulating the polarization state. The polarization angle is rotated by a zero-order half-wave plate and a polarizing beamsplitter is used to separate the polarized light into its horizontal, or P, and vertical, or S, components. The vertical component, which has a slightly higher reflectance by metal mirror surfaces mounted on the table top and positioned at an angle of 45° relative to the beam path, is deflected toward the microscope. Rotation of the output polarization from horizontal to vertical, via rotation of the half-wave plate, increases the intensity of the light deflected to the microscope according to the cosine of the angle. Lastly, we note for completeness that intensity control on the millisecond time scale can be achieved using a scheme in which a birefringent plate is mounted to a fast optical scanner (W. Denk, patent pending).

A fraction of the laser light is used for beam diagnostics. A first glass slide positioned at 45° relative to the beam is used to pick off roughly 4% of the beam power and deflects it to a PC-based spectrometer via a fiber optic cable. A second glass slide is used to pick off an additional roughly 4% of the beam power and deflects it to a photodiode as a relative measure of the intensity of the laser output.

Here, as in general, the pick-off should be located downstream of the intensity control mechanism but upstream of the shutter.

Either a two-lens or four-lens telescope is used to reshape the laser beam for input to the microscope as required. The output of the Ti:Sapphire laser has a 1.7-milliradian (full-angle) divergence and an initial beam diameter of $D_{beam} = 0.7$ mm. This is reshaped to a beam diameter equal to that of the scan mirrors (i.e., $D_{SM} \simeq 4$ mm), with an f = +25-mm and +100-mm pair as well as a dual f = +50-mm pair for the case of a four-lens telescope.

A mechanical shutter is placed in the beam path just before the beam is deflected upward by a periscope toward the scan mirrors (Figure 6.15). The shutter position is computer controlled and, for safety reasons, its default position in the absence of electrical power blocks the beam from the scanners.

As a practical issue, for purposes of alignment we use iris diaphragms as variable apertures to define the height and position of the beam. Unless otherwise stated, all mirrors have a flat, protected silver surface and are held in standard kinematic mounts. Certain mirrors are placed on translation stages for transverse alignment. Last, safety precautions must be maintained in the use of laser light for TPLSM. Thus, black anodized metal shields are used to surround the scanners and some optics located near normal eye level.

6.4.4 PATH ALONG MICROSCOPE: EXCITATION

The microscope is built as a tripod with X-95 optical rail (Figure 6.16). One leg serves as an optical bench, and the other two legs serve as supports. A customized adapter atop the tripod serves to connect the legs. A pair of mirrors mounted at 45° is used as a periscope to steer the beam to the height of the scan mirrors. The top periscope mirror mount is connected horizontally to the main X-95 rail and angled at 45°. The laser light deflected from the top periscope mirror travels horizontally to the alignment mirror and then to the two scan mirrors. The laser light then travels downward through the scan lens, the tube lens, and the dichroic beamsplitter before being focused by the objective onto the preparation (Figure 6.17).

There are five main attachments to the main X-95 rail (Figure 6.17). At the top, two carriages are attached, one in front and one in back. The front carriage holds the scanners and an alignment mirror, and the back carriage holds the top half of the periscope. The next attachment is the scan lens mount. A 100%/0% switchable trinocular headstage, which provides the eyepieces for visual inspection of the preparation and holds the tube lens, is mounted on a separate X-95 carriage below the scan lens. The bottom attachment is a modular focusing unit, to which the detector assembly and the objective holder are mounted. Last, the sample stage allows for "x" and "y" translation of the preparation and sits directly on the air table.

6.4.4.1 Optical Scanner

The back X-95 carriage holds the top mirror of the periscope. An L bracket attaches to the mirror mount and holds it in the appropriate orientation (Figure 6.17). The front X-95 carriage is connected to a rod assembly that holds both the scanners and

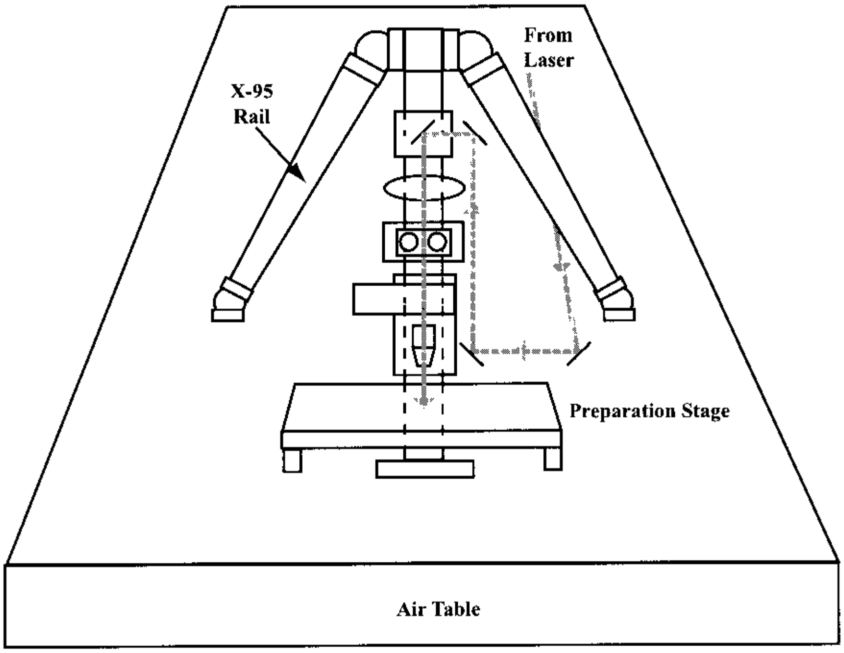

FIGURE 6.16 Illustration of the physical superstructure of the two-photon laser-scanning microscope. The tripod is constructed of X-95 rail; the front leg forms the optical rail of the microscope and the side legs act as supports. The incident laser path is shown in gray.

an alignment mirror (Figure 6.18). The alignment mirror is located at the orthogonal intersection point of the planes defined by the periscope mirrors and the first scan mirror. The scanners are mounted in a small, orthogonally positioned mirror assembly that is an accessory to the scanners. The mirror assembly is attached to a custom-designed, water-cooled base that, in turn, is attached to the rod assembly; water cooling is necessary only for large scan angles at the highest speeds, an atypical situation. The rod assembly itself consists of seven posts, i.e., 2 of 8 in., 4 of 6 in., and 1 of 4 in., and seven cross-post adapters.

6.4.4.2 Scan Lens

The scan lens is a 1.0× magnification Plan-Apo dissection microscope lens (Leica). It is held and centered on a custom-designed mount and attached to the main X-95 carriage. A major consideration for the design of the scan lens holder is mechanical stability, and thus our mount is reinforced with diagonal bracing.

6.4.4.3 Headstage

The headstage is an upright trinocular (Zeiss) in which the phototube pathway is used as the laser beam pathway. The headstage contains a 100%/0% beam switcher that is used to change between visual inspection with the binocular and laser-

The headstage is an upright trinocular (Zeiss) in which the phototube pathway is used as the laser beam pathway. The headstage contains a 100%/0% beam switcher that is used to change between visual inspection with the binocular and laser-

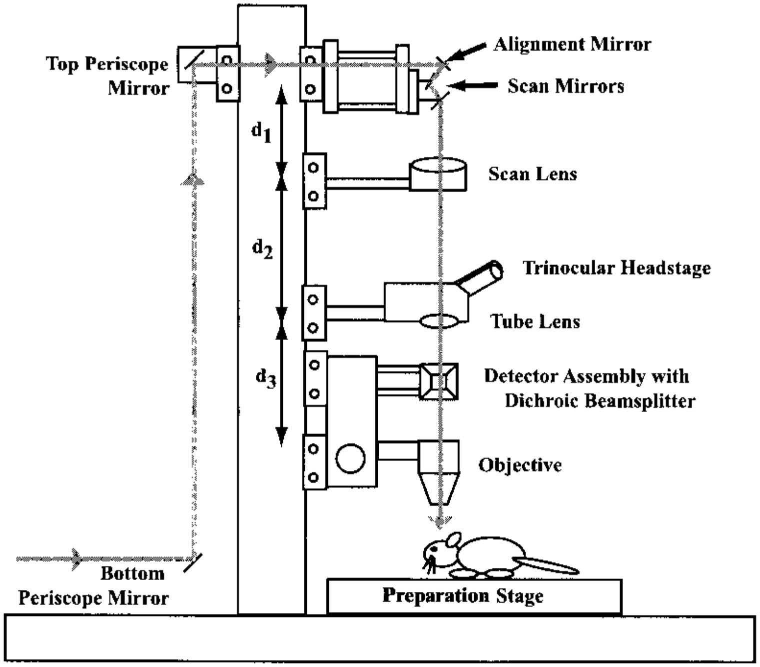

FIGURE 6.17 The main attachments to the main X-95 rail in the two-photon laser-scanning microscope. The laser pathway from the periscope to the objective along the optical rail that forms the microscope includes the alignment mirror, the scan mirrors, the scan lens, the tube lens, and the detector assembly. The collection optics for the fluorescent light are not shown. The values of the separation distances for our system are d_1 = 114.5 mm, d_2 = 252.7 mm, and d_3 = 95 mm.

scanning microscopy. The trinocular contains an f_2 = +160-mm tube lens that is used as the second lens of the scan system telescope. The trinocular is directly mounted to the custom-designed headstage adapter, reinforced with diagonal bracing, that is in turn mounted on an X-95 carriage.

6.4.4.4 Focusing Stage

Axial alignment of the objective is achieved with a commercial modular focusing unit (Nikon). This unit allows 30 mm of vertical motion, which facilitates changing preparations and objectives. A custom-made adapter plate is attached to the focusing unit and the objective holder is mounted to the adapter plate. The objective holder consists of a custom-made groove plate and five Microbench™ (Linos Photonics) parts in the configuration shown in Figure 6.19.

6.4.5 PATH ALONG MICROSCOPE: DETECTION

6.4.5.1 Detector Assembly

The detector assembly is attached to the focusing unit via the adapter plate. The entire detector assembly is placed on a slider plate so that the dichroic beamsplitter

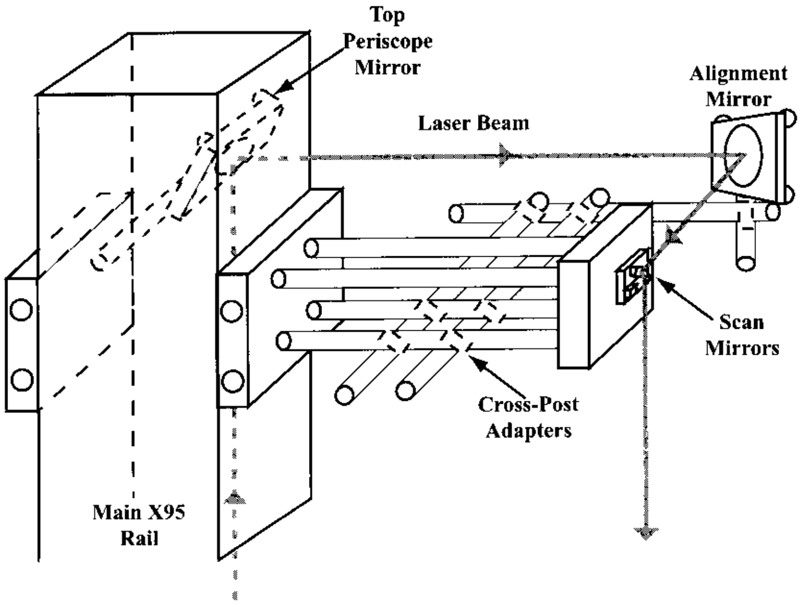

FIGURE 6.18 The uppermost attachments to the X-95 rail that forms the microscope. The attachment at the rear holds the top periscope mirror. The attachment at the front holds the rod assembly and is constructed of stainless steel posts, right-angle cross-post adapters, and an X-95 carriage that connects to the scan mirrors and the alignment mirror.

can be removed from the visual path and then replaced without changing its alignment relative to the other collection optics. The back panel of a slider plate is mounted to the adapter plate, and a Microbench™ mounting plate is attached to the front panel of the slider plate. Four rods inserted into the mounting plate are used to attach the detector assembly by its rear left face.

The detector assembly is constructed mainly with Microbench™ parts in a double-cube configuration (Figure 6.20a). Nine square plates are formed into a rectangle using four long rails and two short rails. Two $f_{CL} = +27$-mm lenses serve as the collectors and are loaded into the far right plate and the right rear plate. Eight 2-in. rods are inserted into the same plates to provide a mounting area for the glass filters and detectors. Infrared blocking filters and appropriate bandpass filters are mounted in additional square plates that slide directly onto the rods. The PMT detectors are mounted in a customized holder (Figure 6.20b), which also slides directly onto the rods.

The two dichroic beamsplitter mirrors, one of which separates the incident laser light from the emitted fluorescent light (beamsplitter #1) and one of which resolves the fluorescent light into separate spectral bands (beamsplitter #2), are held on prism mounts inserted through the front left plate and bottom right plate. The laser enters through the top left plate and exits through the bottom left plate of the double cube. The far left plate, front right plate, and the open top right region are covered with black tape to block stray light from reaching the detectors.

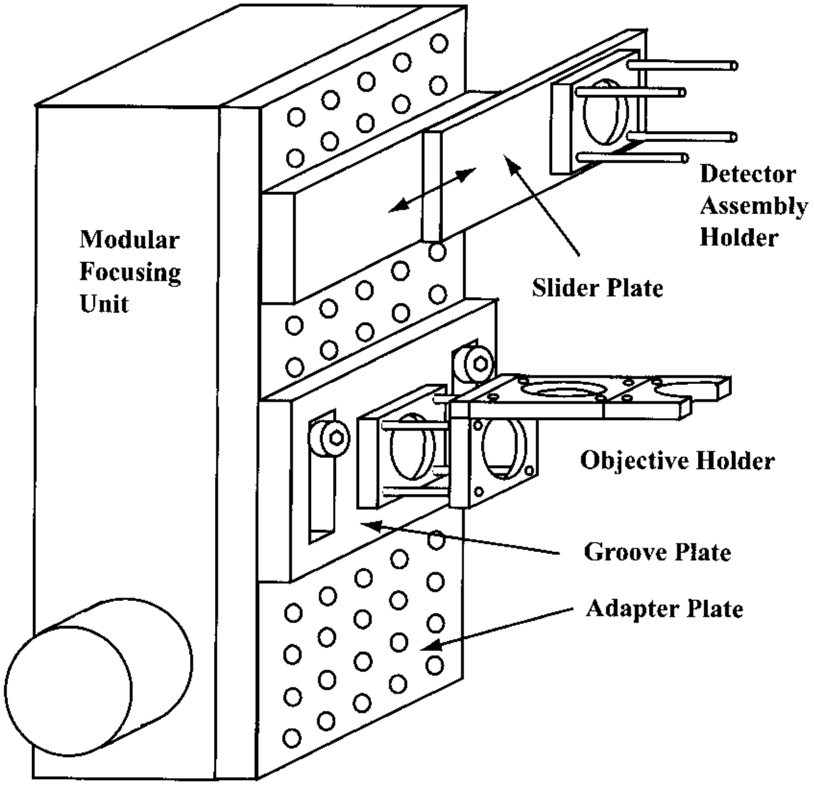

FIGURE 6.19 The focusing unit that supports the objective and detector assembly on the main X-95 rail. The objective holder consists of Microbench™ parts (Linos Photonics) connected to a modular focusing unit (Nikon) by two custom-made plates; an adapter plate with 1/4-20 holes spaced on ½-in. centers that is driven by the modular focusing unit, and a groove plate that supports the objective holder. The detector assembly holder consists of a slider plate and Microbench™ parts and is mounted on the adapter plate.

6.4.5.2 Collection Optics

The first element in the collection pathway (Figure 6.21) is the long-pass dichroic beamsplitter mirror, i.e., λ_{cut} = 600-nm DCLP, that transmits light at the laser excitation wavelength while deflecting fluorescent light toward the detectors. A second dichroic may be used, if necessary, to separate the fluorescent signals from two different fluorescent indicators. For example, we use a λ_{cut} = 505-nm DRLP to resolve light from yellow fluorescent protein (YFP) vs. cyan fluorescent protein (CFP). The signal in either path is then focused onto the active area of a PMT by a short-focal-length lens. A laser-blocking filter, comprising 2 mm of Corning no. BG40 glass, is used to further reduce the background level and associated noise caused by scattered incident laser light. Additional filters are placed in front of the detector as is appropriate for the given experiment, e.g., λ_{pass} = 525 ± 5 nm to isolate YFP and λ_{pass} = 485 ± 11 nm to isolate CFP.

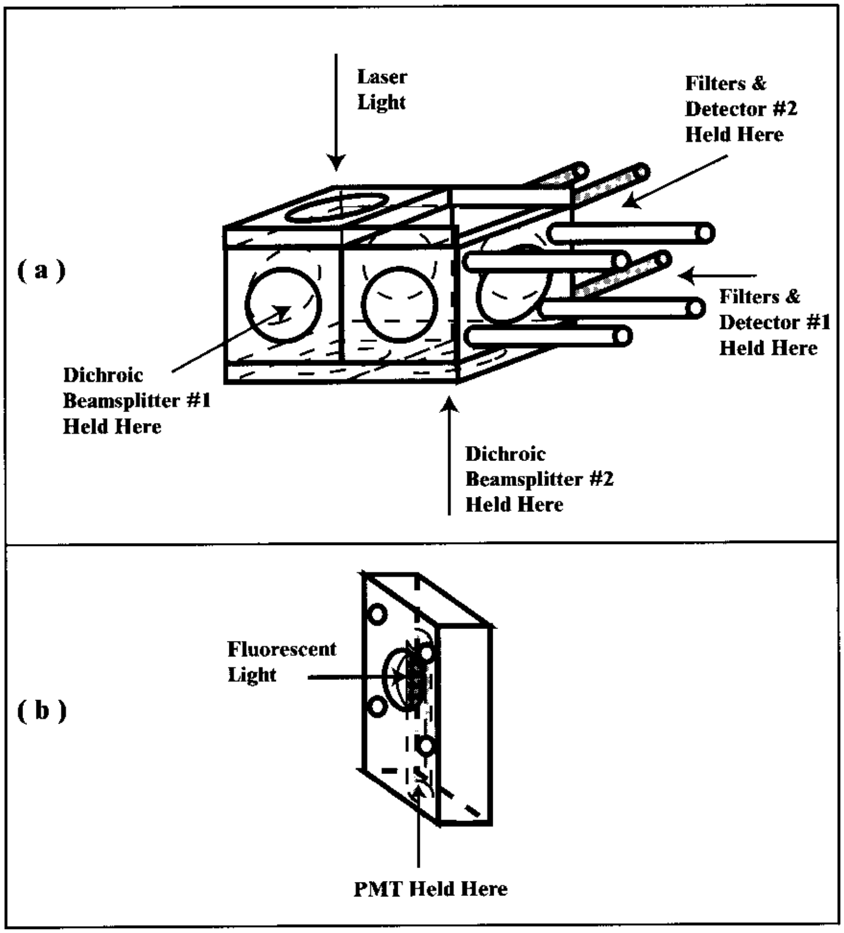

FIGURE 6.20 Illustration of the detector assembly. (a) The main assembly is fabricated from Microbench™ parts. Dichroic beamsplitters are mounted on adjustable prism mounts and placed in the labeled openings. Filter blocks and the photomultiplier tubes (PMTs) are held by the four rods protruding along each path. (b) The PMT case is a custom-made aluminum cage designed to be compatible with Microbench™ parts and the compact Hamamatsu PMTs.

In the collection assembly, an $f_{CL} = +27$-mm lens of $D_{CL} = 30$-mm diameter is placed at $l_1 = 120$ mm from the back aperture of the objective and at $l_2 = 35$ mm from the detector. In this configuration, the back aperture is imaged onto the detector surface with a magnification of 0.29×. Therefore, a $D_{BA} = 8$-mm back aperture is imaged to a 2.3-mm diameter circle at the PMT active surface.

6.4.5.3 Photodetectors

The detectors in our system are Hamamatsu R6357 photomultiplier tubes. We chose these PMTs because of their spectral properties, high sensitivity, and relatively small

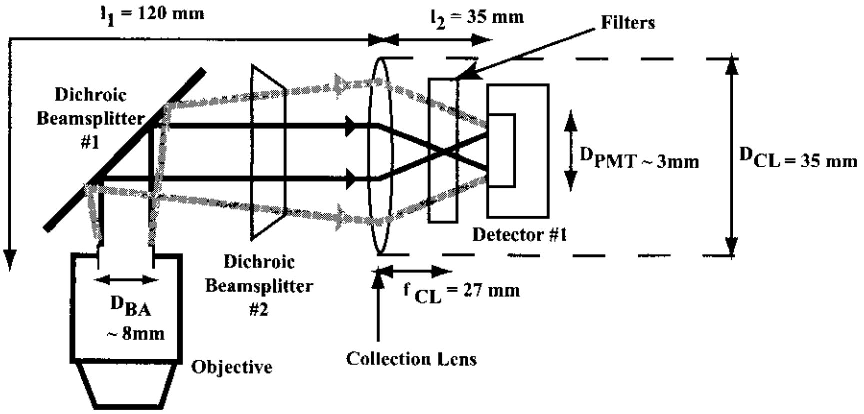

FIGURE 6.21 Detailed schematic of the detector assembly. The positions of both dichroic beamsplitters are shown; however, for clarity we omit the optics and detector for the second, otherwise equivalent, pathway. Unscattered fluorescent light is depicted as dark lines, while scattered fluorescent light is depicted as gray lines.

size. They are powered by adjustable high-voltage supplies. The output of each PMT is converted to a voltage with a current-to-voltage converter of local design (no. OPA111 operational amplifier, Burr Brown) with a measured time constant of $\tau = 0.8$ µsec and adjustable conversion gains of 1×10^4 to 8×10^4 V/A. An alternative and possibly superior solution is to use a charge-to-voltage switched integrator gated by the pixel clock of the acquisition program.

6.4.6 SCAN AND ACQUISITION ELECTRONICS

The scanners and associated electronics and computer boards must be chosen and configured to provide horizontal and vertical scans that are synchronized to each other, so that they define a raster, as well as to the data acquisition. Additionally, in order to make the scan and acquisition run independently of the computer's CPU, both the scan functions and the acquisition function should be synchronized to a pixel clock on one of the computer boards, as depicted in Figure 6.22.

6.4.6.1 Scan Mirrors and Drivers

We use state-of-the-art galvanometer optical scanners from Cambridge Technology Inc. (model 6210). These scanners are capable of rotations up to ± 20° and rates of up to 1.7 kHz at reduced deflection angles. We typically use angles of ± 5° or less; for a 40× magnification, deflections of ± 1° correspond to distances of ± 40 µm in the focal plane. The scanners hold $D_{SM} = \simeq 4$ mm aperture mirrors (6 min at 45°) provided by the manufacturer. Each scanner is driven by a MicroMax™ Series 670 Single Axis Board Level Mirror Positioning System that takes a standard analog ±10-V signal as the input and transforms the voltage into an angle.

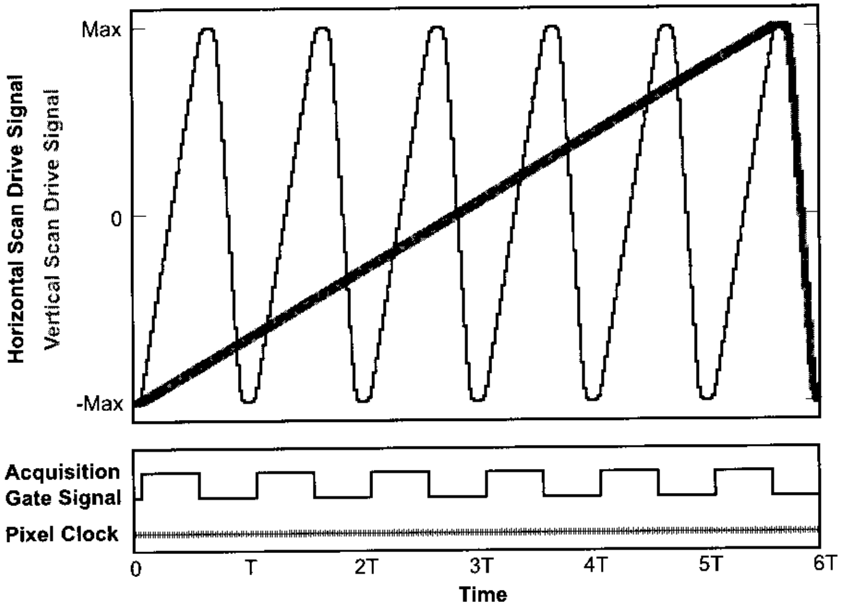

FIGURE 6.22 Cartoon illustration of the drive signals for the scan mirrors and data acquisition over the period of a full frame of acquisition. The time is in units of horizontal scan periods, denoted T. All functions are synchronized to the continuously running pixel clock. The data acquisition gate is active for a portion of the fast horizontal scan. During this time window, data are acquired at the pixel clock rate. The horizontal (fast) scan signal is updated with each pixel clock tick, while the vertical (slow) scan signal is updated once per fast scan cycle. The number of steps and the number of horizontal scans per vertical scan have been greatly reduced for illustrative purposes.

6.4.6.2 Computer Cards

The horizontal- and vertical-scan system is composed of a scan generator consisting of a pair of National Instruments model PCI-6711 analog output boards. The horizontal- and vertical-scan boards have first-in-first-out (FIFO) memories so that one-dimensional waveforms may be downloaded to the boards. The boards can then be commanded to transmit those waveforms repetitively. Digital counters, also located on the boards, can be programmed to set up the sync functions, so that the horizontal and vertical scans will run in a synchronized manner. Although each board has four analog output channels, the PCI-6711 has only a single common clock and a single common FIFO memory. Therefore, two boards are needed for very fast scan operation. Eight digital output lines are also available on each board, which may be used for various control output functions such as a shutter control for the laser.

Data acquisition is performed by a National Instruments model PCI-6110E four-channel analog input board. Two channels are used for the two photomultipliers and two are reserved for electrophysiological data or additonal detectors. This board has four independent analog-to-digital converters. Therefore, it can acquire data at very fast rates and directly stream the data into memory. The board is synchronized with the two scan boards (Figure 6.22).

The three interface boards communicate with each other via the real-time system integration (RTSI) bus accessed via a connector on the top surface of the board (Table 6.2). A 34-pin cable connects all of the RTSI bus lines. The pixel clock, line clock, and frame clock signals from the raster generator are passed to the PCI-6110E, so that data collection is automatically synchronized to the scan (Figure 6.22). The host computer needs only to manage the data flow.

The scan and acquisition software sets up the control counters and downloads the scan waveforms to the respective boards. The start signal is then issued from the host machine, and the horizontal generation begins and repeats continuously without any further intervention by the software. This method of semiautonomous operation allows instrument operation and data collection to occur in a manner independent of the processor speed of the computer. The computer needs only to have enough memory to buffer the data. Alternately, the data can stream directly to disk, depending on the data rate required for a particular experiment.

6.4.6.3 LabVIEW™-Based Software

The scan and data collection system is controlled by a master program written in LabVIEW™ 5.1. At the start of the program, the ramp is generated by means of a LabVIEW™ subroutine. The ramp waveform is divided into six separate sections: a rising cubic acceleration region, a rising linear region, a rising cubic deceleration region, a falling cubic acceleration region, a linear falling region, and a falling cubic deceleration region. The ends of the separate regions match in value and slope so that a continuous, smooth waveform is formed (Figure 6.22). The resulting waveform reduces the slew rate of the signals that will be applied to the mechanical scanners and thus facilitates the fastest possible scan rates. The horizontal waveform is calculated by means of a FOR LOOP with six separate paths, selected in turn as the FOR LOOP steps from zero to the final value, which is the number of pixels desired for one line. Each path is constructed out of standard LabVIEW™ mathematical components. The vertical waveform utilizes the same waveform calculation method; the period of the vertical waveform must be a multiple of the period of the horizontal waveform. For each board, the AO Config.vi routine supplied by LabVIEW™ is used to assign the on-board FIFO memory that stores the calculated waveform values.

Each of the scan boards has a system timing controller circuit, denoted as the DAQ STC, that makes a common set of control signals available on each board (Table 6.2). Thus, the control signals and the counter signals from one board are available to the other boards via common connections provided by the RTSI bus. In addition to the control signals, each DAQ STC circuit provides two counters and eight general-purpose digital I/O lines. The RTSI bus carries various control and clock signals as well as eight lines, designated RTSI 1 through 8, that are software assigned by the user. Most of the I/O and control signals for each of the counters can be assigned to any of the RTSI bus lines.

For the horizontal-scan ramp, the route signal.vi routine supplied by LabVIEW™ is used to assign the AO update signal to one of the RTSI lines, i.e., RTSI 4. This

TABLE 6.2
Assignments for National Instruments Boards

Real-Time System Integration (RTSI) Bus Assignments

RTSI #	Signal	Source	Purpose
4	Pixel clock	Board #1	Master clock for counters in the scan generators
3	Pixel clock gate	Board #3	Asserts the start of an acquisition period during a horizontal scan
2	Frame clock	Board #1	Asserts the beginning of each frame
1	Line clock	Board #2	Asserts the beginning of each line scan

Connection Assignments

Board #	Name	Board Connection	Function
1	Horizontal scan generator (PCI-6711)	Counter 0 input	Counts down line clock (Input from RTSI #1)
		Counter 0 output	Generates frame clock (Output to RTSI #2)
		Analog output DAC0	Horizontal scan signal
2	Vertical scan generator (PCI-6711)	Counter 0 input	Counts down pixel clock (Input from RTSI #4)
		Counter 0 output	Generates line clock (Output to RTSI #1)
		Analog output DAC0	Vertical scan signal
		Digital I/O output 0	Shutter control
3	Analog input (PCI-6110E)	Counter 0 input	Counts down pixel clock (Input from RTSI #4)
		Counter 0 output	Generates pixel clock gate (Output to RTSI #3)
		Counter 0 gate	Gated by line clock (Input from RTSI #1)
		Trigger 1	Acquisition gate (Input from RTSI #3)
		Startscan	Acquisition clock (Input from RTSI #4)
		Digital I/O lines 0–4	Output to focus stepper motor controller
		Analog input 0	Detector, PMT #1
		Analog input 1	Detector, PMT #2
		Analog input 2	Reserved for electrophysiological data or optional detector
		Analog input 3	Reserved for electrophysiological data

signal serves as the system master pixel clock. Counter 0 on the vertical-scan board is initialized with the index value of the horizontal-scan generator and then counts down the pixel clock, which reaches zero at the end of the horizontal scan. This way, the counter generates an output pulse when the horizontal scan completes. This signal is called the line clock and is assigned to RTSI 1 by means of the route signal.vi routine. By means of the down counter.vi routine, the line clock signal is used as the update clock for the vertical-scan ramp generator. Note that, as distributed by National Instruments, the down counter.vi cannot be assigned to a signal on the RTSI bus. To modify the routine, access the diagram of the down counter.vi, remove the case structure associated with the time-base assignments, and configure the cluster containing the time-base source and time-base signal so that these two parameters are selected by inputs to the routine. This way, these parameters can be selected in the main vi routine. The time-base source is set to 6, which selects the RTSI, and the time-base signal is set to the desired RTSI pin.

With the scan boards configured as indicated, the horizontal-scan generator is the master and the vertical-scan generator is synchronized to the horizontal-scan pixel clock and steps up every time the horizontal-scan ramp completes one cycle. Thus, the horizontal-scan and vertical-scan ramps are always synchronized (Figure 6.22). In a similar manner, counter 0 is initialized with the vertical-scan ramp index value and counts down the line clock on RTSI 1, so the resultant output is triggered when the vertical-scan ramp finishes. This signal is called the frame clock and, by means of a route signal.vi, is attached to RTSI 2. As configured, pixel clock, line clock, and frame clock are all available on the RTSI bus.

Analog data collection is best understood by assuming that the horizontal-scan and vertical-scan ramps are both active and that the pixel clock, line clock, and frame clock are being generated. Using a modified delayed pulse config.vi routine supplied by LabVIEW™, counter 0 is arranged so that it is gated when line clock is asserted and then begins counting the pixel clock on RTSI 4 until the horizontal ramp reaches the desired value. Then the counter 0 output, denoted by the pixel clock gate and assigned to RTSI 3, opens the analog gate. Data collection is clocked by the pixel clock and is initiated by gating the pixel clock on RTSI 4 via the Startscan input. Then counter 0 is reset by the pixel clock gate and begins counting pixels until the requested number of data points has been reached. Then the output of counter 0 turns off the analog data collection using the delayed pulse config.vi routine. The horizontal scan generator completes the scan and then resets, and the process begins again. The delayed pulse config.vi routine is modified in the same manner as the down counter.vi routine. The diagram is modified by removing the structure in front of the time-base source and time-base signal cluster and adding direct assignments, i.e., for RTSI 4.

The analog data are read by using the services of the AI read.vi routine and displayed by using the National Instruments IMAQ™ imaging software. AI read.vi generates a two-dimensional array of data, but that array is not in a form suitable for generating a display since it contains no horizontal-scan indexing information. One solution is to place the AI read.vi routine in a FOR LOOP indexed by the number of lines in each frame. The AI read.vi is commanded to read the pixel data for one scan line; a complete frame of data from the input buffer is acquired by calling the routine at each cycle of the FOR LOOP. For display purposes, one channel is selected from the AI read output array by means of the index array.vi routine. This effectively converts the two-dimensional array to a one-dimensional array, formed back into a two-dimensional array as the index values are automatically incremented by the FOR LOOP as the array passes through the loop boundary. The array is presented to the array-to-image.vi routine, along with an image definition from the create image.vi routine. The image data then pass to the windraw.vi routine that displays the image on the monitor screen.

When the main program is started, the sub vi routine calculates the horizontal-scan and vertical-scan values, the boards are programmed, and the various counters are initialized. Then the system stops and waits for the start signal. All functions receive a common start so that all operations start together and remain synchronized. Once started, the horizontal-scan and vertical-scan ramps operate without using any control signals. The computer resources can then be devoted to managing data collection and storage and the display monitor. The system also waits for the stop button to initiate a controlled shutdown procedure. In shutdown, all the counters are cleared along with the RTSI bus lines, which allows a fresh start.

6.4.7 FOCUS CONTROL

It is often desirable to step along the focus axis either as a means to automate the choice of focal plane or to acquire a set of successive images systematically. The modular focus unit is easily coupled to a stepping motor by capturing the fine focus knob in a friction-held cap. The motor is a two-phase stepping motor with two windings driven by an SN754410 (Texas Instruments) motor driver integrated circuit. The motor signals for the driver are generated in a LabVIEW™ sub program that allows both manual and automatic stepping. To increase the angular resolution, the stepping motor is operated in half-step mode, so the stepping pattern is 4 bits wide and 8 bits long. The pattern is installed in an eight-element array by means of the build array.vi routine. The eight steps described in binary are:

Step 0: 1000
Step 1: 1001
Step 2: 0001
Step 3: 0101 (6.19)
Step 4: 0100
Step 5: 0110
Step 6: 0010
Step 7: 1010

In automatic mode, one of the counters in one of the DAC STC chips is used to count the frame clock and the counter value is then converted to modulo 8 by means of a LabVIEW™ math function. The resultant number varies between zero and seven and is used to index the array by means of the index array.vi. If the reverse motion is desired, a formula node is used to subtract the value from seven before indexing. For manual mode, the stepping is controlled by switches on the

means of a LabVIEW™ math function. The resultant number varies between zero and seven and is used to index the array by means of the index array.vi. If the reverse motion is desired, a formula node is used to subtract the value from seven before indexing. For manual mode, the stepping is controlled by switches on the

LabVIEW™ front panel that enable a FOR LOOP that steps from zero to seven once every 0.1 sec. The stepping pattern selected is presented to the DIO write.vi and the DIO start.vi routines. The 4 bits then appear on four lines of the digital port selected by the port config.vi routine; a fifth line is used as an on/off control (Table 6.2). Each binary bit corresponds to a single pin of the port.

In this scheme, reading the counter is done after the image is displayed and stored. In the unfortunate event that the data rate is high and the computer processor speed is slow, the counter may increment more than once before being read. In an unusual case such as this, it might be necessary to implement control of the stepping motor with hardware.

6.4.8 IMAGE ROTATOR

For many experiments it is desirable to rotate the image. For example, in line-scan operation, in which the vertical-scan axis is degenerated into a single line, image rotation allows the region of interest to be aligned along the horizontal-scan axis. The image is rotated by reorienting the raster scan. The rotation is performed in hardware by four analog multipliers arranged in a rotation matrix, wired to conform to

$$\begin{aligned} X' &\leftarrow X\cos\Theta - Y\sin\Theta \\ Y' &\leftarrow X\sin\Theta + Y\cos\Theta \end{aligned} \tag{6.20}$$

where X and Y are the original horizontal- and vertical-scan waveforms, X′ and Y′ are the rotated horizontal- and vertical-scan waveforms, and Θ is the desired rotation angle. The sinΘ and cosΘ terms are calculated by a microprocessor, converted to analog by digital-to-analog converters, and presented to the analog multipliers. Two more multipliers are used, one in each output channel, to act as gain controls. The system is capable of rotation by any angle without limitation. The microprocessor is controlled by means of a keypad and a rotation control knob; the operation status is displayed on a liquid crystal display panel. This system is similar to all-analog designs implemented in the past.[44] The virtue of the present system is the use of a single knob and keypad for ease of control and the use of an external serial RS232 input to the microprocessor to give the main LabVIEW™ program control of the rotator as well.

6.5 PERFORMANCE AND APPLICATIONS

6.5.1 SYSTEM VALIDATION

After our system was constructed and tested, various calibrations were performed to determine the true lateral resolution, axial resolution, exact values of scale factors, and uniformity of the image.

6.5.1.1 Spatial Scales

The horizontal and vertical scale factors are determined by imaging a circular opening of known diameter, as shown for a 50-μm metal pinhole illuminated with

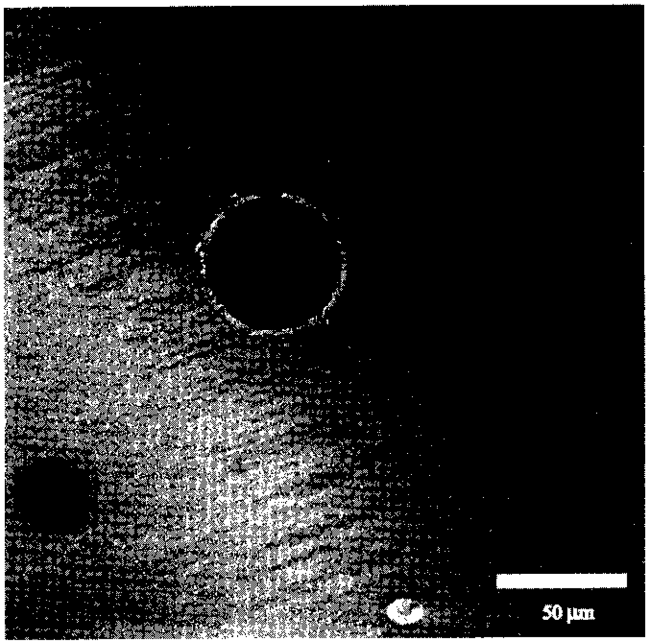

FIGURE 6.23 Image of an aperture used to calibrate the lateral dimension of our two-photon laser-scanning microscope. The aperture corresponds to a 50-μm pinhole and the contrast is generated by reflected light from the polished metal surface.

800-nm light (Figure 6.23). No fluorescent dye is used; the reflected light from the polished surface is sufficiently strong so that enough 800-nm light leaks through the dichroic beamsplitter and blocking filters to provide a signal. The diameter along the horizontal and vertical axes, as measured in pixels, yields the scale factor at a particular zoom setting. As the image is best viewed without distortion, the gain for the horizontal and vertical directions should be identical and can be adjusted via the digital multipliers in the "rotator box." This calibration is repeated at several magnifications to ensure the linearity of the scale factor as a function of magnification.

6.5.1.2 Resolution

The resolving power of the microscope can be determined by imaging fluorescent beads whose diameter is below the optical resolution limit. The beads must be dilute, so that an individual bead can be identified, and they should be suspended in agarose to reduce motion during imaging. Figure 6.24 contains an image of 0.2-μm yellow-green fluorescent microspheres (Polysciences Inc., PA), suspended in 2% agarose, that was obtained with our microscope using a 40× water immersion objective (Zeiss). The full width at half-maximal intensity from individual beads in the lateral dimension was calculated from the acquired images (Matlab™; Mathworks, MA). The axial resolution is obtained by compiling a series of images taken at different axial positions and calculating the intensity profile of a single bead as a function of axial position. We determined that the spatial resolution (FWHM) for our system was

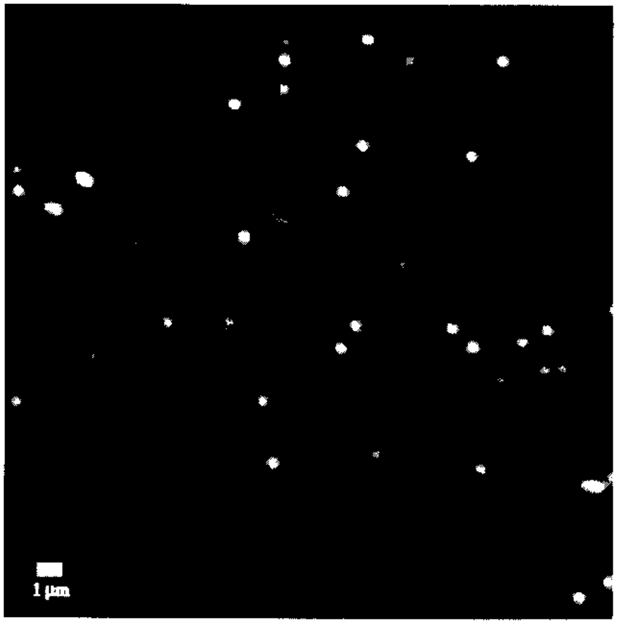

FIGURE 6.24 Image of fluorescent microspheres used to establish the resolution of our two-photon laser-scanning microscope. The microspheres are 0.2-μm latex balls (no. 17151; Polysciences, Inc., Warrington, PA) coated with fluorescein.

$$d_{\text{lateral}} \cong 0.5\ \mu\text{m} \quad \text{and} \quad d_{\text{axial}} \cong 2\ \mu\text{m}$$

These are consistent with the calculated, worst-case values (Equations 6.4 and 6.5) and a previous characterization.[45]

6.5.1.3 Spatial Uniformity

The homogeneity of the scan was determined by imaging a spatially uniform field of fluorescence, i.e., a Petri dish filled with a 100-μM solution of fluorescein. This method detects inhomogeneities in the detection pathway as well as in the scan pathway. The profile obtained in this manner, shown in Figure 6.25, is observed to be asymmetric and to decay more extensively, by nearly 20% over 100 μm along some directions, than the prediction for the scan pathway alone (Figure 6.11). Nonetheless, the profile is stable for a given configuration of the microscope, the intensity profile in the central 100 μm of the field is uniform to within 10%, and the measured profile can be used as a calibrated filter for images taken with this system. Postprocessing with this filter yields a fluorescent image free of spatial intensity distortions.

6.5.2 PULSE WIDTH

The shape and duration of the incident laser pulse critically affects the efficiency of nonlinear optical processes (Figure 6.3). The ultrashort pulses used for multiphoton

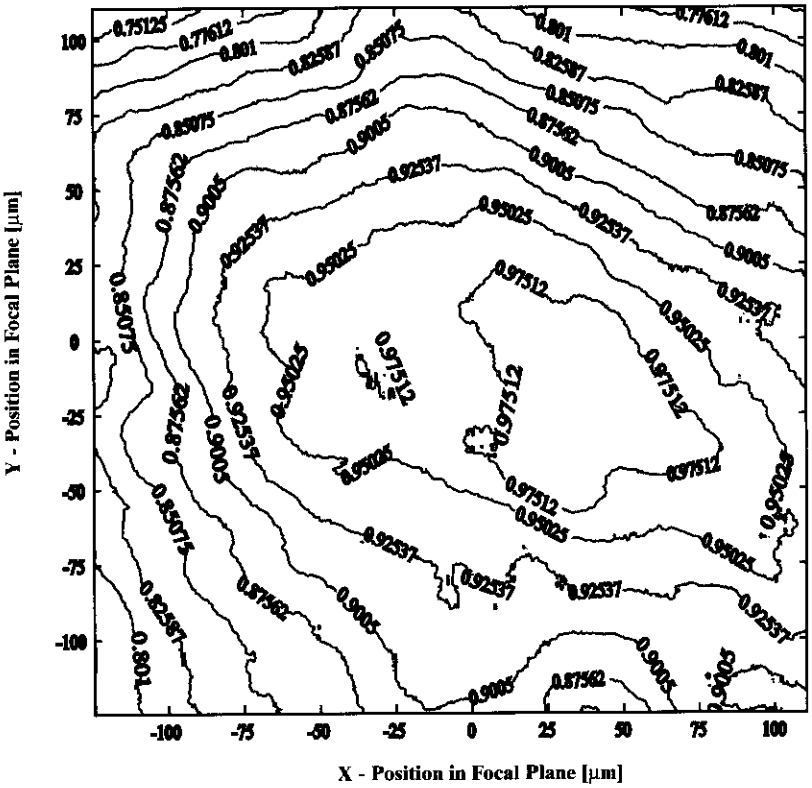

FIGURE 6.25 Contour plot of the spatial uniformity of the measured two-photon fluorescence measured with a 40× magnification lens. Note that the decrement across the entire field is due to both nonideal scanning and detection conditions and exceeds that calculated for the scanning alone (Figure 6.11). The decrement across the central 100 μm of the field is less than 10%.

microscopy are typically one hundred to a few hundred femtoseconds in duration. Since no electronic photodetector has the necessary time resolution to measure such time scales, optical pulse measurement techniques must be used. An autocorrelation measurement is an effective and relatively simple method of monitoring the pulse length.

6.5.2.1 Autocorrelation

In an autocorrelation measurement, a laser pulse is split into two identical copies. One pulse is delayed relative to the other by a time τ, which results in two pulses with electric fields $E(t)$ and $E(t + \tau)$. The two pulses are recombined and used to excite a nonlinear process such as two-photon fluorescence. The interferometric autocorrelation function, denoted $I_{AC}(\tau)$, is given by the sum of $E(t)$ and $E(t + \tau)$, raised to the fourth power and averaged over time. This appears as an oscillatory signal with an envelope that depends on the delay time τ (Appendix B). A convenient

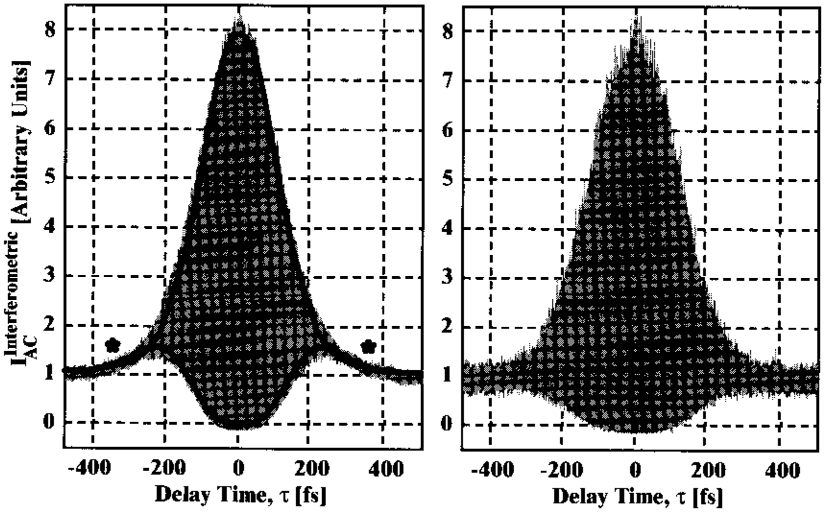

FIGURE 6.26 The interferometric autocorrelation function measured for laser pulses at the focus of the objective with our two-photon laser-scanning microscope. (a) The autocorrelation under typical levels of performance. The asterisks indicate additional curvature as a result of chirp in the pulse. The envelope of the autocorrelation is fit with the calculated autocorrelation for a chirped pulse (thick envelope), from which we estimate the FWHM of the laser pulse to be 250 fsec. The chirp parameter is $b = 5 \times 10^{-5}$ $fsec^{-2}$; this corresponds to a fractional shift in frequency of $2 \times b \times \tau_p^{FWHM} \times \omega = 0.01$, with $\omega = \lambda_0/2 \times \pi \times c$, where $\lambda_0 = 800$ nm and c is the speed of light. (b) The autocorrelation for a pulse with essentially no chirp, i.e., $b \cong 0$. For this case we estimate the FWHM of the laser pulse to be 180 fsec (Equation A5).

feature of this autocorrelation is an 8:1 ratio of the amplitude of the maximum from zero to the amplitude of the constant background produced by widely separated pulses. Achieving this ratio indicates that the apparatus is well aligned. In the case that the laser pulse has essentially no chirp, the FWHM of the autocorrelation is equal to 1.7-times the FWHM of the intensity of the original pulse.

Our laser system and microscope were set up without external pulse compression. We constructed an autocorrelator that could be switched into the beam path (Figure 6.15), as described.[46,47] We found that, although the commercially purchased Ti:Sapphire laser should output pulses around 120 fsec, pulses at the microscope objective are typically closer to

$$\tau_p^{FWHM} = 250 \text{ fsec}$$

as shown by a fit of a model autocorrelation (Appendix B) to the measured autocorrelation function (Figure 6.26a). This pulse is chirped, as evidenced by the curvature in the wings of the autocorrelation function (* in Figure 6.26a). The increase in pulse width represents the cumulative effect of optics throughout the entire TPLSM system (Figure 6.15). By judicious tuning of the laser, we could achieve pulses without chirp and with widths of $\tau_p^{FWHM} = 180$ fsec (Figure 6.26b and Equation A5).

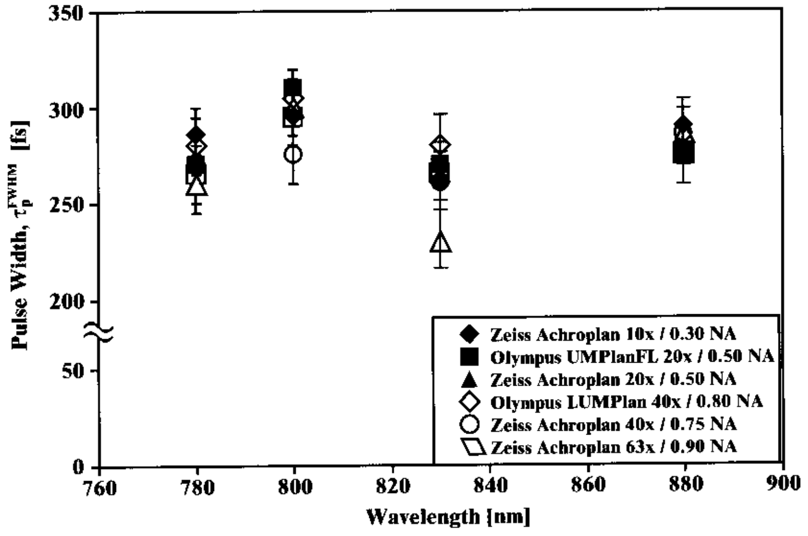

FIGURE 6.27 Plot of the FWHM of the laser pulse measured for six different common objectives as a function of excitation wavelength. There is no significant difference in pulse width between lenses or as a function of frequency.

6.5.2.2 Comparison of Objectives

To compare the performance of various brands and types of objectives, each with different glasses and detailed construction, identical laser parameters were measured using a number of objectives on the microscope. We found that the variations of the measured pulse width from the objectives were not significant at a given wavelength and no significant change in pulse width over the 780- to 880-nm range of wavelengths for the incident light (Figure 6.27) occurred.

6.5.2.3 Effect of the Scan Lens

One concern in the construction of the microscope is dispersion in the large amount of glass of the scan lens that is required to achieve superior off-axis optical characteristics. Pulse widths were compared for measurements with the normal scan lens (Leica, Appendix A) in place as opposed to a thinner achromat used as a scan lens. With the initial pulse width near $\tau_p^{FWHM} = 250$ fsec, and for wavelengths near 790 nm, we found that the use of an achromat shortens the pulse width to $\tau_p^{FWHM} = 230$ fsec. This is less than a 10% improvement at the cost of decreased off-axis optical quality. For comparison, removal of the scan lens and the tube lens so that only the objective remains in the pathway results in a value of $\tau_p^{FWHM} = 180$ fsec.

6.5.3 TWO-PHOTON SPECTRA

Single-photon excitation spectra have been published for most common dyes and can be experimentally obtained with a noncoherent source. In contrast, the two-

6.5.3 TWO-PHOTON SPECTRA

Single-photon excitation spectra have been published for most common dyes and can be experimentally obtained with a noncoherent source. In contrast, the two-

photon excitation spectra of relatively few molecules have been published to date. Two-photon excitation spectra cannot be trivially derived from their corresponding single-photon excitation spectra, partially due to different quantum selection rules governing one- vs. two-photon absorption. Therefore, two-photon excitation spectra must be determined experimentally whenever one uses a new dye or indicator.

We constructed a spectrophotometer to measure the two-photon action spectra, i.e., the extent of integrated fluorescence, as a function of the excitation wavelength. The spectrum is uncompensated for the relative extent of radiative vs. nonradiative decay. It is obtained by measuring the two-photon excited fluorescence from an unknown sample relative to that of a dye with a known two-photon spectrum[48]; in our case we used fluorescein at pH 11 (the tabulated spectrum for pH 13[49] matches an earlier measurement taken at pH 11[48]). The measurements are performed and compared on a wavelength-by-wavelength basis; thus, the final action spectrum does not depend on detailed knowledge of the pulse characteristics of the laser (Figure 6.28a and Appendix C). For most fluorescent studies, in which the signal is based on the amount of generated fluorescence, the action spectra contain more relevant information than the excitation spectra. On the other hand, for certain photobleaching experiments, the actual excitation spectra may contain the more relevant information.

The two-photon action spectrum of the fluorescent dye, cascade blue, is shown in Figure 6.28b (dark lines and symbols). Superimposed on the graph (gray lines and symbols) is the published two-photon excitation spectrum of the dye taken by direct measurement. The two curves are well matched to within a scale factor, i.e., the two-photon fluorescent efficiency. This result demonstrates the validity of the comparative method. The two-photon spectra for yellow fluorescent protein (YFP) and cyan fluorescent protein (CFP) are shown in Figure 6.28c. These two genetically encodable variants of green fluorescent proteins are used in several physiological indicators, e.g., Ca^{2+}-sensitive probes,[50,51] that can be delivered by viral vectors.

6.5.4 *IN VITRO* [CA^{2+}] MEASUREMENTS

We describe the use of our two-photon laser-scanning microscope to probe the change in internal calcium concentration of plated HeLa cells infected with the Ca^{2+}-sensitive cameleon protein via an adenovirus vector.[52] Cameleon is a chimeric protein that consists of two genetically encodable fluorophores, CFP and YFP, separated by a calcium-binding protein complex derived from calmodulin;[50] the spectra of these fluorophores are described in Figure 6.28c. At low calcium concentrations, the fluorophores are held distal from one another, and excitation of the cyan fluorophore results primarily in emission characteristic of CFP. At high calcium concentrations, the calcium-induced conformational change of calmodulin brings the two fluorophores in close proximity to each other. This allows fluorescence resonance energy transfer to occur from the cyan to the yellow fluorescent protein. In this conformation, excitation of the cyan fluorophores results in some emission characteristic of yellow fluorescent protein. The ratio of the two emission signals can therefore be used as an indicator of calcium concentration.

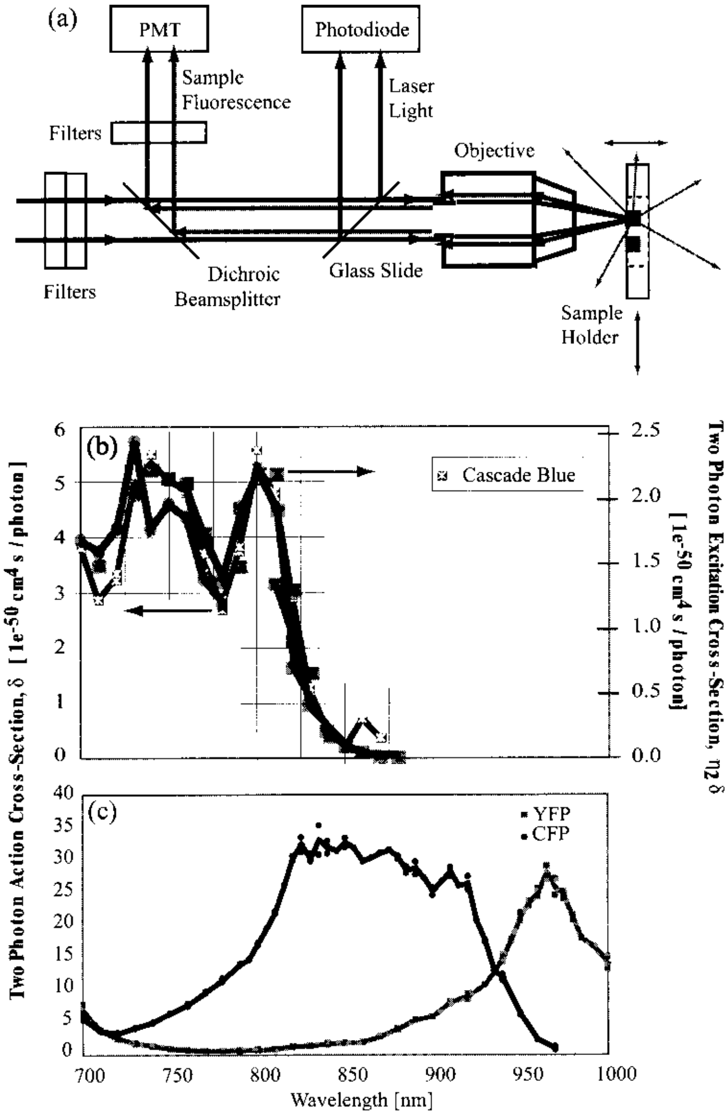

FIGURE 6.28 Two-photon action spectra. (a) Schematic of the two-photon spectrometer. The laser light path is represented by dark lines and the fluorescence detection pathway is represented by gray lines. The test sample is depicted as a gray box and the reference sample is depicted as a dark box. The samples can be translated in the axial direction and one lateral direction as a means to make sequential measurements of the two samples and thus compare their relative two-photon generated fluorescence. (b) Two-photon action spectrum of cascade blue (black symbols and connecting lines). The published two-photon excitation spectrum[48] is shown for comparison (gray lines). The relative scale between the two data sets was chosen to match the two curves. (c) The two-photon action spectra for the genetically encodable yellow fluorescent protein (YFP; gray squares) and cyan fluorescent protein (CFP; dark circles). The lines connect the average of the data values at each wavelength.

The images shown in Figures 6.29a and 6.29b correspond to the fluorescence from HeLa cells that express cameleon. The image shown in Figure 6.29a is formed from emission centered on 485 nm and represents a mixture of emission from the CFP and the YFP, with the dominant emission from the CFP. The image shown in Figure 6.29b corresponds to fluorescence centered on 525 nm and consists primarily of emission from yellow fluorescent protein. A change in calcium concentration may be induced in HeLa cells by the bath application of histamine, which triggers an intracellular release of calcium. This change may be quantified by measuring, for the 485-nm and 525-nm bands, the integrated fluorescence in a region of interest vs. time. These signals are shown in Figure 6.29c; note the counter-correlated signal change in the two wavelength bands. The ratio of the two fluorescent signals is clearly seen to increase in response to the histamine application.

6.5.5 *IN VIVO* CORTICAL BLOOD FLOW

A unique aspect of TPLSM is the ability to observe anatomical and functional signals in the brains of living animals deep to their pial surface.[3] As an example, we consider the flow of blood in individual capillaries in rat cerebral cortex[2] (Figure 6.30). A cranial window is prepared over whisker barrel sensory cortex, the dura is removed, and a metal frame and closed surgical window are attached to the skull for stable mounting of the preparation to the microscope table.[20] The blood stream is labeled with fluorescein isothiocyanate-dextran (77 kD). A single optical section obtained 100 μm below the pial surface is shown in Figure 6.30a; the maximal projection reconstructed from 41 individual images, ranging in depth from 80 to 120 μm below the pial surface of the brain, is shown in Figure 6.30b. Individual red blood cells appear in the capillaries as dark stripes that correspond to locations where the fluorescent dye was excluded from the vessel during the scan. Depending on the optical properties of the preparation, images from depths exceeding 600 μm have been achieved using TPLSM.[30] It may also be possible to image flow in individual capillaries through a thinned but intact skull.[53]

Line scans may be taken repeatedly along an individual capillary to produce a continuous measure of blood flow (Figure 6.31). The spatial coordinate is taken to be along the direction of the scan, while the perpendicular direction represents the temporal coordinate. As the blood cell moves along the capillary, its position along the line scan changes from scan to scan, thereby tracing out a dark line, as shown for three examples (Figures 6.31a to 6.31c). The data of Figure 6.31a show continuous flow; analysis of these data provides information regarding three parameters of capillary blood flow: blood cell speed, blood cell flux, and blood cell linear density, where flux = linear density × speed. The slope of the line is the inverse of the instantaneous speed; i.e., speed = $|dt/dx|^{-1}$. The spacing between the lines along the temporal coordinate direction is a measure of the cell flux, while the spacing between the lines along the spatial coordinate direction is a measure of the cell density. The line scan data of Figure 6.31b contain a short vertical region, indicative of a momentary stall of the red blood cells, while those of Figure 6.31c illustrate some of the high variability in flow that may be observed.

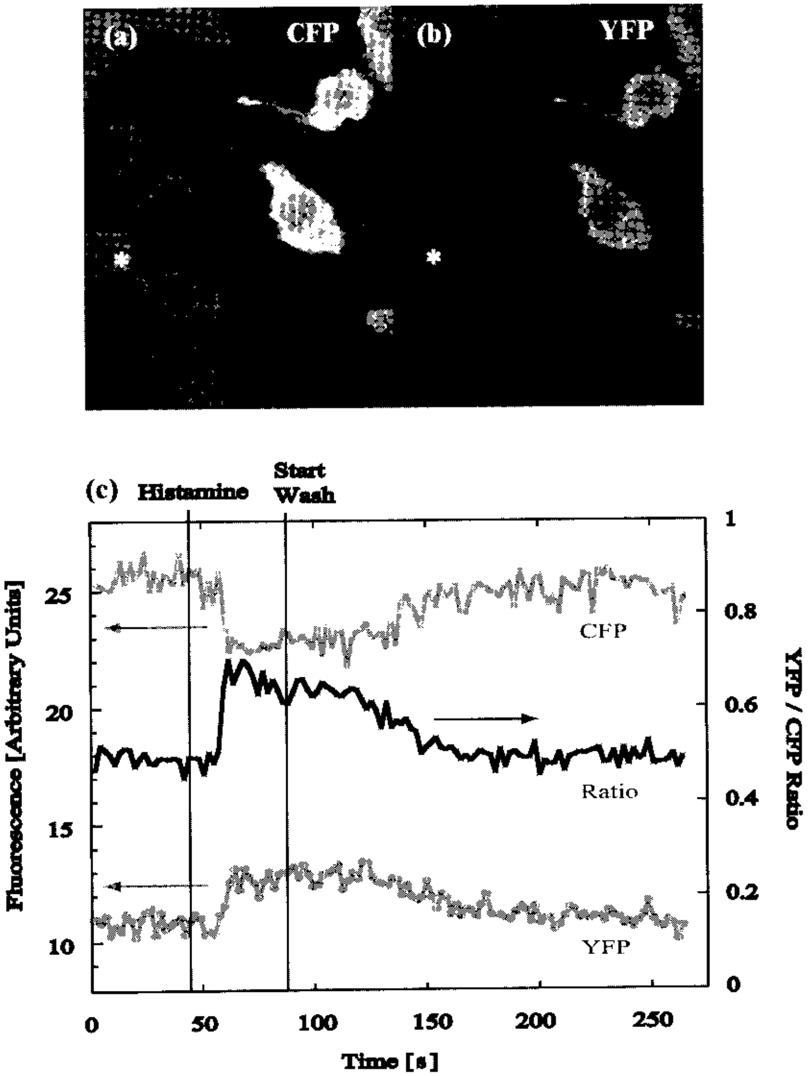

FIGURE 6.29 *In vitro* TPLSM used to measure Ca^{2+} dynamics in HeLa cells infected with the cameleon protein construct via an adenovirus vector. (a) Image of the HeLa cells at emission wavelengths centered on 485 nm. The majority of the emission that forms the image is from cyan fluorescent protein. (b) The same field simultaneously imaged at emission wavelengths centered on 525 nm. Almost all of the emission that forms the image is from yellow fluorescent protein. (c) Graph of intensity vs. time in channels centered on 485 and 525 nm for an isolated region of interest, designated by the * in parts a and b, as a function of time. Also shown (dark line) is the ratio of the two channels. Bath application of 100-μM histamine was used to trigger an intracellular release of free Ca^{2+}. Note the counter-correlated signal change in the two channels and the resultant increase in the fluorescent ratio in response to the histamine application. The initial emission values are seen to recover subsequent to a wash with saline.

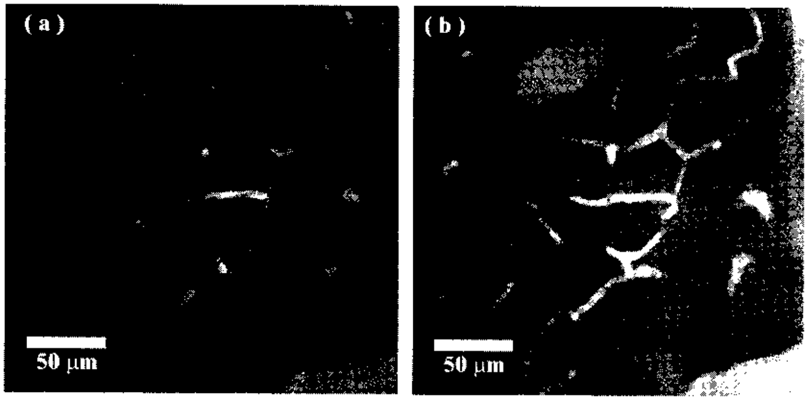

FIGURE 6.30 *In vivo* TPLSM used to image a capillary bed in rat vibrissa primary sensory cortex. An optical window was prepared over this region and the blood stream was labeled with 77-kD fluorescein conjugated-dextran. (a) A single planar image from a depth of 100 μm below the pial surface of cortex. Notice that individual red blood cells, which occlude fluorescent dye, appear in the capillaries as dark stripes. (b) A maximal projection reconstructed from 41 planar images, as in part a, taken between 80 and 120 μm below the pia.

APPENDIX A: PARTS AND VENDORS FOR THE TPLSM

MECHANICAL

The 8 × 4 × 1 ft anti-vibration air table was purchased from Newport (Irvine, CA). For mirror mounts, we used the Ultima® series from Newport and the Flipper Mounts from New Focus (Santa Clara, CA). All mirror mounts were attached to standard ½-in. posts and post holders from Newport held to the air table with clamping plates and forks from New Focus. Microbench™ parts were obtained from Linos Photonics (Milford, MA). The large X-95 rails and assorted clamps and brackets were purchased from a variety of vendors. Crossed roller bearing translation stages were obtained from Newport, the slider for the detector assembly was from New England Affiliated Technologies (SD Series; Lawrence, MA), and the Modular Focusing Unit was obtained from Nikon (part no. 883773; Garden City, NY).

OPTICAL

All mirrors were λ/10 flatness, protected silver mirrors obtained from Newport. Water-immersion objectives were purchased from Zeiss (Thornwood, NY) and Olympus. Blocking filters were obtained from Andover Corporation (Salem, NH), while dichroic beamsplitters and interference filters were from Omega Optical Inc. (Brattleboro, VT) and Oriel Instruments (Stratford, CT). The wave plate, polarizing beamsplitter, and intermediary optics were obtained from Newport and Linos Photonics. The scan lens, a Plan-Apo 1.0× magnification dissection stereoscope objective (focal length of 92.7 mm, physical length of 60 mm, and measured front and back working distances of 56 mm) was from Leica (McBain Instruments, Chatsworth, CA).

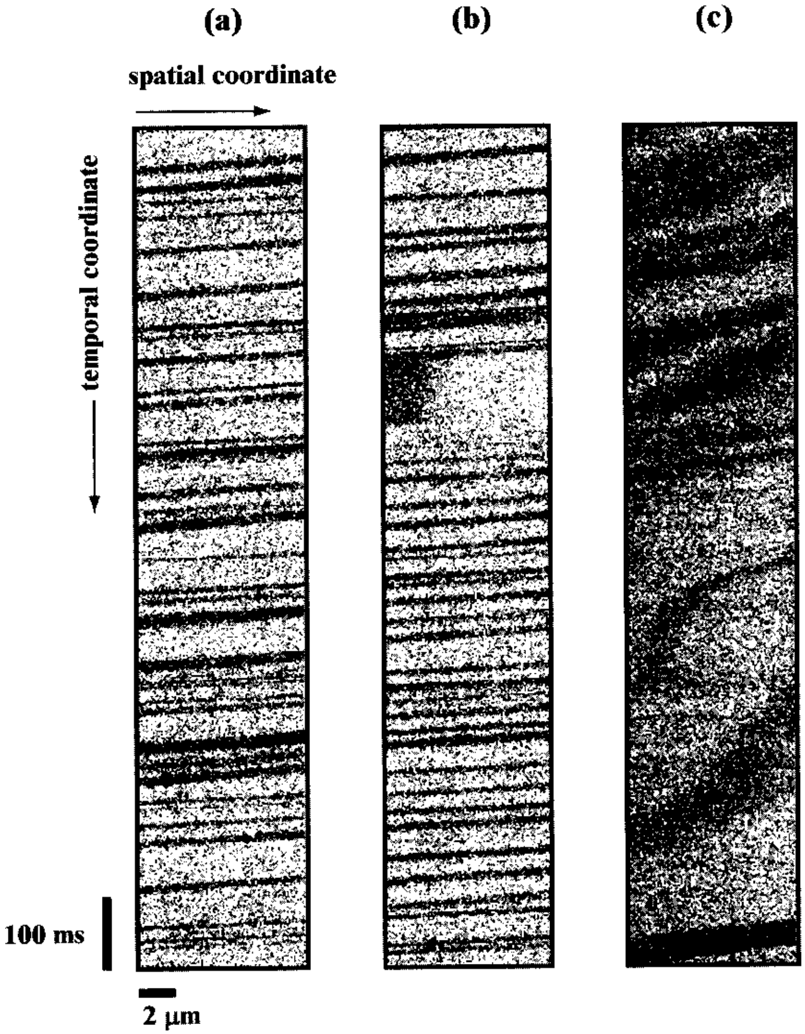

FIGURE 6.31 *In vivo* TPLSM used for functional imaging of capillary blood flow. Shown are line scan data taken along single capillaries in rat vibrissa primary sensory cortex through an optical window, as in Figure 6.30. The motion of red blood cells appears as dark stripes against a bright plasma background in these time-space plots of repeated line scans through the capillary; see text for details. (a) Relatively uniform flow. The thickness of the dark lines may reflect the orientation of the red blood cell. (b) Flow that is interrupted by a brief stall. (c) Flow that is highly irregular and that changes in speed within the field of view.

SCANNERS

The scanning galvanometers and their drivers were obtained from Cambridge Technologies (Boston, MA). The scanners are Model 6210 Galvanometer Optical Scanners capable of ±20° maximum deflection. They have a 300-μsec set time. We used

MicroMax™ 670 scan drivers, which take a ±10-V analog input. The power supplies for the scan drivers were obtained from Acopian (Easton, PA).

PHOTOMULTIPLIER TUBES

The detectors in our system were selected for high sensitivity with low dark current (model R6357 specified for dark currents below 2 nA; Hamamatsu Corporation, Bridgewater, NJ). Each photomultiplier tube is powered by a model E850-13 base (Hamamatsu Corporation) that is energized with a 0- to 2000-VDC adjustable power supply (Model PMT-20C-N; Bertan Associates, Hicksville, NY), although the tube is used only below the maximum rating of 1250 V required for this particular PMT.

ELECTRONICS

The waveform generator for the scanning galvanometers consists of two model PCI-6711 Arbitrary Waveform Boards from National Instruments (Austin, TX). The data acquisition board is a model PCI-6110E four-channel analog input board from National Instruments. The stepping motor that controls the axial translation of the focus is a Vexta model PH268M-M1.5 (Herbach and Rademan Company, Moorestown, NJ). It has 400 steps per revolution, which results in 0.25-μm axial steps in combination with the modular focusing unit.

LASER AND ANCILLARY EQUIPMENT

The Ti:Sapphire laser is a Mira-900 (Coherent Laser Group, Santa Clara, CA) equipped with a broadband mirror set. The pump laser is a Verdi-V10 (Coherent Laser Group) 10-W pump laser. Two chillers (NESLAB Instruments, Portsmouth, NH) are required for stable temperature operation of the laser and are supplied by Coherent. The spectrometer consists of a PC2000-ISA computer card (Ocean Optics Inc., Dunedin, FL) and an associated fiber optic cable. The fast oscilloscope used to monitor the repetition rate of the Ti:Sapphire laser is a 400-MHz Tektronix model TDS430A oscilloscope (Newark Electronics). The infrared viewer is a Find-R-Scope from FJW Optical Systems, Inc. (Palatine, IL). The photodiode used to monitor the average laser power is a Si-based PIN diode obtained from Hamamatsu Corporation. A calibrated energy meter (model 818T-10, Newport) is used to calibrate the photodiode.

APPENDIX B: BASICS OF INTERFEROMETRIC AUTOCORRELATION

In the autocorrelation process the laser pulse is split into two identical copies and one is delayed relative to the other by a time τ. This results in two pulses with electric fields $E(t)$ and $E(t + \tau)$. These are subsequently multiplied together through a nonlinear process such as two-photon excitation. For such a process, the instantaneous two-photon excited fluorescence for a given delay time is

$$I(t,\tau) = \left|[E(t) + E(t+\tau)]^2\right|^2 \tag{A1}$$

The time resolution of the photodetector is much slower than the fluorescence duration; thus, the output of the photodiode is the time average of I(t, τ) (Equation A1). This signal corresponds to the autocorrelation function, $I_{AC}(\tau)$; i.e.,

$$I_{AC}(\tau) = \int_{-\infty}^{\infty} dt \left|[E(t) + E(t+\tau)]^2\right|^2 \tag{A2}$$

To deduce the shape of the original pulses from the autocorrelation signal $I_{AC}(\tau)$, we assume a known original pulse shape. The autocorrelation signal can be calculated in terms of parameters describing the original pulse. The measured autocorrelation signal shape can then be used to deduce the original pulse parameters. Ultrashort laser pulses usually have Gaussian or secant-squared time envelopes. Since the Gaussian is a good estimate of the actual pulse shape and facilitates calculations, we assume a Gaussian profile for our beam. The electric field of the laser pulses can be described as

$$E(t) = E_0 \exp\left\{-\frac{t^2}{a^2} + i\omega t\right\} \tag{A3}$$

where the full-width-half-maximum (FWHM) of the envelope of the intensity of the pulse is $a\sqrt{2\ln 2}$, ω is the center wavelength of the pulse, and the origin of time is arbitrary, as E(t) and E(t + τ) appear only in integrals over all of time, e.g., Equation A2.

The autocorrelation measurement can be set up in two ways. In an interferometric autocorrelation, fringes caused by the interference of the two pulses are observed. The two pulses are incident on the fluorescent material so that they are exactly colinear and are polarized in the same direction. In a noninterferometric autocorrelation, the fringes are smeared out either by introducing an angle between the beams or a difference in the polarization direction of the two pulses. While both autocorrelation methods give a measure of pulse length, the interferometric autocorrelation will also indicate the presence of chirp in the pulse.

The interferometric autocorrelation signal with E(t) given by Equation A3 is

$$I_{AC}^{\text{interferometric}}(\tau) \propto 1 + 2e^{-\frac{\tau^2}{a^2}} + 4e^{-\frac{3\tau^2}{4a^2}}\cos(\omega\tau) + e^{-\frac{\tau^2}{a^2}}\cos(2\omega\tau) \tag{A4}$$

The upper envelope and lower envelope can be found by setting ωτ = π or 2π. A convenient feature of interferometric autocorrelation is the 8:1 ratio of the amplitude of the maximum from zero to the amplitude of the constant background. Achieving this ratio indicates that the apparatus is well aligned. In the case with

A convenient feature of interferometric autocorrelation is the 8:1 ratio of the amplitude of the maximum from zero to the amplitude of the constant background. Achieving this ratio indicates that the apparatus is well aligned. In the case with

unchirped pulses, the FWHM of $I_{AC}^{interferometric}(\tau)$, denoted τ_{AC}^{FWHM}, is related to the FWHM of the original pulse by

$$\tau_{P}^{FWHM} \approx \sqrt{\frac{ln2}{2}} \cdot \tau_{AC}^{FWHM} \tag{A5}$$

In the presence of chirp, the interferometric autocorrelation function develops curvature in the wings of the signal (* in Figure 6.26). When this feature is present, the FWHM of the autocorrelation and the original pulse no longer have the simple relation given by Equation A5. The central peak of the autocorrelation signal will become narrower because the red-shifted, leading portion of the pulse will only incompletely interfere with the blue-shifted tail. The electric field of a linearly chirped pulse can be described as

$$E(t) = E_0 \exp\left\{-\frac{t^2}{a^2} + i\omega t - ibt^2\right\} \tag{A6}$$

where b is a measure of the chirp. The experimentally obtained autocorrelation must be fit to the autocorrelation that is calculated (Equations A2 and A6) with the two parameters, a and b, taken as variables in order to determine the pulse length. In practice, for two-photon microscopy an absolute measurement of the chirp is generally not necessary. One typically adjusts only the laser to minimize the curvature in the wings of the autocorrelation signal.

APPENDIX C: SPECTROMETER FOR TWO-PHOTON ACTION SPECTRA

The high optical intensities necessary for generation of significant two-photon excitation typically require a pulsed laser source. The Ti:Sapphire is one of few currently available pulsed lasers tunable over a wavelength range that is suitably large for spectroscopy. Unfortunately, the pulse characteristics of this laser do not remain constant as it is tuned from 700 to 1000 nm. Two-photon excitation is extremely sensitive to changes in the pulse width and pulse shape of the laser output. Thus, a direct measurement of a two-photon-induced excitation spectrum would require that the pulse characteristics be simultaneously monitored, such as with an autocorrelation technique (Appendix B). On the other hand, two-photon excitation spectra can be obtained without detailed knowledge of the pulse characteristics by comparing the two-photon excitation spectrum of an unknown sample with that of a dye of known two-photon spectrum. Direct measurements of the two-photon excitation spectra for some common dyes have been reported by Xu.[7] Based on this past work, our two-photon excitation spectrometer is designed to take measurements against dyes of known two-photon spectra.

The comparative method for obtaining two-photon excitation spectra makes the assumption that the pulse characteristics do not fluctuate significantly over the time scale of the measurement at any given wavelength and output power of the laser. Although characteristics of the laser will change as the laser is retuned, the measurement of the test sample is taken directly after measurement of the reference sample at each wavelength without retuning the laser between the two measurements. Thus, although the exact pulse characteristics are unknown and may differ between wavelengths, they are the same for both samples at any given wavelength.

The excitation cross section for the test sample at a given wavelength can be calculated by taking the ratio of its collected fluorescence to that collected from the reference sample and multiplying by the known excitation cross section of the reference sample. If the emission spectra of the test and reference samples are different and the efficiencies of the objective, dichroic beamsplitter, detector, or filters differ for the two emission spectra, then these efficiencies ratios must also be factored into the final calculation.

DESIGN

The design of the comparative two-photon excitation spectrometer is shown in Figure 6.28A. The laser light passes through a long-pass dichroic beamsplitter, chosen to transmit the laser wavelengths and reflect the fluorescent signals. A portion of the laser beam is deflected to a photodiode to monitor the average laser power. The remainder of the beam passes to the objective and is focused into the sample, which is free to translate both laterally and in the axial direction. The transmission curve of the dichroic is typically not constant across the tunable laser wavelengths. It is, therefore, important that the photodiode pick-off is placed after the dichroic so that it monitors the actual laser power transmitted to the objective. Small inaccuracies in the average power reading do not affect the two-photon spectra, as the average power is used solely to check that the fluorescent signal varies with the square of the incident power and thus verify that neither the dye nor the PMT are saturated.

CONSTRUCTION

The frame for the two-photon spectrometer is built primarily from Microbench™ parts. The dichroic beamsplitter and glass slide are mounted on prism mounts. The objective is held horizontally by a threaded Microbench™ plate and the filters, photodiode, and PMT are mounted in Microbench™ parts and attached via protruding rods (Figure 6.20B). The sample holder is a single-axis Microbench™ translation stage situated to move in the transverse direction. The sample holder is part of a spring-loaded translation assembly that allows translation in the axial direction.

The samples are held in microslide cuvets (VitroCom Inc; Mountain Lakes, N.J.) with inner dimensions of 0.1 × 2.0 mm, chosen to minimize the sample volume. The microslides are held with bone wax to a 25-mm adapter plate (Microbench™) in which we machined parallel grooves for the microslides to seat. An OG590 colored glass filter (Oriel Instruments) was placed at the entrance of the spectrometer to prevent single-photon excitation by residual 532-nm light from the pump laser. We use a 600-DCLP dichroic beamsplitter (Omega Optical Inc.) to separate the incident and emitted beams and a BG40 glass filter (Andover Corp.) to block remaining laser light in the emitted pathway. The detector is a Hamamatsu R6353 compact PMT, chosen for its low dark current.

MEASUREMENT PROCEDURES

The microslide cuvets are filled with the test and reference samples, respectively, sealed with bone wax, and placed into the cuvet holder. The cuvets are laterally translated until the beam strikes the center of the reference cuvet. The fluorescent signal from the reference cuvet is then maximized by translating the cuvet in the axial direction. All fluorescent measurements are taken at this axial position. The laser is tuned to a particular wavelength and the fluorescent signal from the center of the reference cuvet is recorded. The cuvets are then laterally translated a predetermined amount so that the beam strikes the center of the test cuvet and the fluorescent signal is recorded. Finally, the samples are translated laterally so that the beam falls between the cuvets and a background reading is taken. The average laser output power is monitored and recorded during each measurement. The laser is then tuned to a new wavelength and this process is repeated.

After the process has been repeated for all desired wavelengths, the laser is tuned to a wavelength at which the excitation of test and reference dyes is reasonably strong. The test cuvet is centered laterally on the beam and the fluorescent signal is recorded. The signal is then maximized in the axial direction. Ideally, the signal should already be maximized, but small variations in the cuvet holder or the cuvet thickness could result in a displacement of the optimal axial positions of the two cuvets. The ratio of the signals taken at the two axial positions is recorded and used to obtain a true test-to-reference fluorescence ratio.

ACKNOWLEDGMENTS

We thank Kerry R. Delaney, Winfried Denk, and Jeffrey A. Squier for useful discussions, Oliver Griesbeck and Roger Y. Tsien for supplying material for the *in vitro* cameleon studies, Samar Mehta for involvement with the spectroscopic measurements, and Kenneth Duff of the Scripps Institute of Oceanography Development Shop for his careful machining. Our work was supported by grants from the David and Lucile Packard Foundation, the NINDS, and, in part, by an NIMH predoctoral training award to Philbert Tsai, an NSF predoctoral fellowship to Nozomi Nishimura, and an NSRA postdoctoral fellowship to Elizabeth Yoder.

REFERENCES

1. Svoboda, K. et al., *In vivo* dendritic calcium dynamics in neocortical pyramidal neurons, *Nature*, 385, 161–165, 1997.
2. Kleinfeld, D. et al., Fluctuations and stimulus-induced changes in blood flow observed in individual capillaries in layers 2 through 4 of rat neocortex, *Proc. Natl. Acad. Sci. U.S.A.*, 95, 15741–15746, 1998.

3. Denk, W. et al., Anatomical and functional imaging of neurons and circuits using two photon laser scanning microscopy, *J. Neurosci. Methods*, 54, 151–162, 1994.
4. Denk, W., Strickler, J.H., and Webb, W.W., Two-photon laser scanning fluorescence microscopy, *Science*, 248, 73–76, 1990.
5. Denk, W., Piston, D.W., and Webb, W., Two-photon molecular excitation in laser-scanning microscopy, in *Handbook of Biological Confocal Microscopy*, Pawley, J.W., Ed., Plenum Press, New York, 1995, 445–458.
6. Denk, W. and Svoboda, K., Photon upmanship: why multiphoton imaging is more than a gimmick, *Neuron*, 18, 351–357, 1997.
7. Xu, C. et al., Multiphoton fluorescence excitation: new spectral windows for biological nonlinear microscopy, *Proc. Natl. Acad. Sci. U.S.A.*, 93, 10763–10768, 1996.
8. Williams, R.M., Piston, D.W., and Webb, W.W., Two-photon molecular excitation provides intrinsic 3-dimensional resolution for laser-based microscopy and microphotochemistry, *FASEB J.*, 8, 804–813, 1994.
9. Soeller, C. and Cannell, M.B., Construction of a two-photon microscope and optimisation of illumination pulse duration, *Pflugers Arch.*, 432, 555–561, 1996.
10. Wier, W.G. et al., A custom confocal and two-photon digital laser scanning microscope, *Am. J. Physiol. Heart Circ. Physiol.*, 278, H2150–H2156, 2000.
11. Denk, W., Two-photon scanning photochemical microscopy: mapping ligand-gated ion channel distributions, *Proc. Natl. Acad. Sci. U.S.A.*, 91, 6629–6633, 1994.
12. Potter, S.M., Two-photon microscopy for 4D imaging of living neurons, in *Imaging Neurons: A Laboratory Manual*, Yuste, R., Lanni, F., and Konnerth, A., Eds., Cold Spring Harbor Laboratory Press, Cold Spring Harbor, New York, 2000.
13. Majewska, A., Yiu, G., and Yuste, R., A custom-made two-photon microscope and deconvolution system, *Pflugers Arch.*, 441, 398–408, 2000.
14. Fan, G.Y. et al., Video-rate scanning two-photon excitation fluorescence microscopy and ratio imaging with cameleons, *Biophys. J.*, 76, 2412–2420, 1999.
15. Lanni, F. and Keller, H.E., Microscopy and microscopic optical systems, in *Imaging Neurons: A Laboratory Manual*, Yuste, R., Lanni, F., and Konnerth, A., Eds., Cold Spring Harbor Laboratory Press, Cold Spring Harbor, New York, 2000.
16. Hiraoka, Y., Sedat, J.W., and Agard, D.A., Determination of three-dimensional imaging properties of a light microscope system. Partial confocal behavior in epifluorescence microscopy, *Biophys. J.*, 57, 325–333, 1990.
17. Agard, D.A. et al., Fluorescence microscopy in three dimensions, *Methods Cell Biol.*, 30, 353–377, 1989.
18. Holmes, T.J. et al., Light microscopic images reconstructed by maximum likelihood deconvolution, in *Handbook of Confocal Microscopy*, 2nd ed., Pawley, J.B., Ed., Plenum Press, New York, 389–402.
19. Neil, M.A.A., Juskaitis, R., and Wilson, T., Method of obtaining optical sectioning by using structured light in a conventional microscope, *Opt. Lett.*, 22, 1905–1907, 1997.
20. Lanni, F. and Wilson, T., Grating image systems for optical sectioning fluorescence microscopy of cells, tissues, and small organisms, in *Imaging Neurons: A Laboratory Manual*, Yuste, R., Lanni, F., and Konnerth, A., Eds., Cold Spring Harbor Laboratory Press, Cold Spring Harbor, New York, 2000.
21. Bailey, B. et al., Enhancement of axial resolution in fluorescence microscopy by standing-wave excitation, *Nature*, 366, 44–48, 1993.
22. Gustafsson, M.G., Agard, D.A., and Sedat, J.W., I^5M: 3D widefield light microscopy with better than 100 nm axial resolution, *J. Microscopy*, 195, 10–16, 1999.

23. Bahlmann, K., Jakobs, S., and Hell, S.W., 1: 4Pi-confocal microscopy of live cells, *Ultramicroscopy*, 87, 155–164, 2001.
24. Born, M. and Wolf, E., *Principles of Optics: Electromagnetic Theory of Propagation Interference and Diffraction of Light*, 6th ed., Pergamon Press, Oxford, 1980.
25. Konig, K. et al., Pulse-length dependence of cellular response to intense near-infrared laser pulses in multiphoton microscopes, *Opt. Lett.*, 24, 113–115, 1999.
26. Centonze, V.E. and White, J.G., Multiphoton excitation provides optical sections from deeper within scattering specimens than confocal imaging, *Biophys. J.*, 75, 2015–2024, 1998.
27. Oheim, M. et al., Two-photon microscopy in brain tissue: parameters influencing the imaging depth, *J. Neurosci. Methods*, 111, 29–37, 2001.
28. Beaurepaire, E., Oheim, M., and Mertz, J., Ultra-deep two-photon fluorescence excitation in turbid media, *Opt. Commun.*, 188, 25–29, 2001.
29. Dunn, A.K. et al., Influence of optical properties on two-photon fluorescence imaging in turbid samples, *Appl. Opt.*, 39, 1194–1201, 2000.
30. Kleinfeld, D. and Denk, W., Two-photon imaging of neocortical microcirculation, in *Imaging Neurons: A Laboratory Manual*, Yuste, R., Lanni, F., and Konnerth, A., Eds., Cold Spring Harbor Laboratory Press, Cold Spring Harbor, New York, 2000, 23.1–23.15.
31. Schonle, A. and Hell, S.W., Heating by absorption in the focus of an objective lens, *Opt. Lett.*, 23, 325–327, 1998.
32. Aquirrell, J.M. et al., Long-term two-photon fluorescence imaging of mammalian embryos without compromising viability, *Nat. Biotechnol.*, 17, 763–767, 1999.
33. Koester, H.J. et al., Ca^{2+} fluorescence imaging with pico- and femtosecond two-photon excitation: signal and photodamage, *Biophys. J.*, 77, 2226–2236, 1999.
34. Piston, D.W. and Patterson, G.H., Photobleaching in two-photon excitation microscopy, *Biophys. J.*, 78, 2159–2162, 2000.
35. Neher, E. and Hopt, A., Highly nonlinear photodamage in the two-photon fluorescence microscopy, *Biophys. J.*, 80, 2029–2036, 2001.
36. Siegman, A.E., *Lasers*, University Science Books, Sausalito, CA, 1986.
37. Bardeen, C.J. et al., Effect of pulse shape on the efficiency of multi-photon processes: implication for biological microscopy, *J. Biomed. Opt.*, 4, 362–367, 1999.
38. Hecht, E., *Optics*, 2nd ed., Addison-Wesley Publishing, Reading, PA, 1987.
39. Fork, R.L., Martinez, O.E., and Gordon, J.P., Negative dispersion using pairs of prisms, *Opt. Lett.*, 9, 150–152, 1984.
40. Trebino, R. et al., Measuring ultrashort laser pulses in the time-frequency domain using frequency-resolved optical gating, *Rev. Sci. Instrum.*, 68, 3277–3295, 1997.
41. Yariv, A., *Optical Electronics*, Holt, Reinehart and Winston, New York, 1985.
42. Wilson, T. and Sheppard, C., *Theory and Practice of Scanning Optical Microscopy*, Academic Press, London, 1984.
43. Mainen, Z.F. et al., Two-photon imaging in living brain slices, *Methods*, 18, 231–239, 1999.
44. Yuste, R. and Denk, W., Dendritic spines as basic functional units of neuronal integration, *Nature*, 375, 682–684, 1995.
45. Soeller, C. and Cannell, M.B., Two-photon microscopy: imaging in scattering samples and three-dimensionally resolved flash photolysis, *Microscopy Res. Tech.*, 47, 182–195, 1999.
46. Muller, M., Squier, J., and Brankenhoff, G.J., Measurement of femtosecond pulses in the focal point of a high-numerical-aperture lens by two-photon absorption, *Opt. Lett.*, 20, 1038–1040, 1995.

47. Diels, J.-C.M. et al., Control and measurement of ultrashort pulse shapes (in amplitude and phase) with femtosecond accuracy, *Appl. Opt.*, 24, 1270–1282, 1985.
48. Xu, C. and Webb, W.W., Measurement of two-photon excitation cross sections of molecular fluorophores with data from 690 to 1050 nm, *J. Opt. Soc. Am.*, 13, 481–491, 1996.
49. Xu, C., Two-photon cross section of indicators, in *Imaging Neurons: A Laboratory Manual*, Yuste, R., Lanni, F., and Konnerth, A., Eds., Cold Spring Harbor Laboratory Press, Cold Spring Harbor, New York, 2000.
50. Miyawaki, A. et al., Fluorescent indicators for Ca^{2+} based on green fluorescent proteins and calmodulin, *Nature*, 388, 882–885, 1997.
51. Romoser, V.A., Hinkle, P.M., and Persechini, A., Detection in living cells of Ca^{2+}-dependent changes in the fluorescence emission of an indicator composed of two green fluorescent protein variants linked by a calmodulin-binding sequence, *J. Biol. Chem.*, 272, 13270–13274, 1997.
52. Miyawaki, A. et al., Dynamic and quantitative Ca^{2+} measurements using improved cameleons, *Proc. Natl. Acad. Sci. U.S.A.*, 96, 2135–2140, 1999.
53. Yoder, E.J. and Kleinfeld, D., Cortical imaging through the intact mouse skull using two-photon excitation scanning microscopy, *Microscopy Res. Tech.*, 56, 304–305, 2002.